Scale Dependence of Parameterizations for Shallow Cumulus Clouds

S. de Boer BSc.

Master's thesis

Supervisors:
Prof. Dr. A.P. Siebesma
Dr. S.R. de Roode

Department of Multi-Scale Physics
Faculty of Applied Sciences
Delft University of Technology

January 29, 2010

Abstract

The largest uncertainty in climate models is caused by cloud feedback. Especially boundary layer (shallow) clouds give a large uncertainty because these clouds need to be parametrized as they are much smaller than the typical gridsize of the large-scale model. The quick improvements of computational power mean that the climate models can be run with a higher resolution. The size of a single gridbox decreases from 50∼25 km to 1∼2 km, which is the same order of size as that of shallow cumulus clouds. The effect of this resolution change on the parametrized variables in shallow cumulus convection is researched in this report with the help of the shallow cumulus Barbados Oceanographic and Meteorological Experiment (BOMEX) case and the Dutch Atmospheric Large-Eddy Simulation (DALES). This LES is used to simulate a single gridbox of the large-scale model (25x25km) and investigate what happens to the variances of several thermodynamic variables, parametrized variables and mean state variables when this domain is divided into subdomains.

It is shown that for all investigated variables no clear dependence on the subdomain size is visible due to a large spread in the variables on the smallest subdomains. This spread can be explained because the smaller subdomains can contain a large or small amount of clouds instead of a large ensemble of clouds as for the full domain, but the average value of the variables over all the subdomains is still very close to the value on the full domain. This means that the parametrization for shallow cumulus convection is still valid when increasing the resolution.

The standard BOMEX case is in a near steady-state and because of this only a small subset of values is observed for the values of the mean state variables, parametrized variables and cloud cover. In order to be able to investigate several relationships between these variables a larger set of values is needed, so the standard BOMEX case is perturbed by changing the initial profiles. It is found that perturbing the relative humidity gives the largest range of values for forementioned variables. Increasing the relative humidity leads to a cloud core mass flux halfway the cloudlayer that can be up to a factor 3 larger than for the original case, and this difference is found to be caused by a change in the cloud core cover. The increased range in values for the cloud core cover are used to show that the parametrization for the cloud core fraction by Neggers et al. (2009) gives a systematic overestimation of the gradient of cloud core cover in the cloud layer for these perturbed BOMEX cases, which means that the cloud fraction in the upper part of the cloud layer is underestimated.

Contents

Chapter 1

Introduction

1.1 Background

Whether it is about the forecast for tomorrow, next week, or predicting climate change over the scale of hundreds of years; climate is important. On a short timescale the weather prediction can for example be needed to know if it is safe to drive, or if airplanes are able to land on the airport. On a longer timescale the influence of humans on the climate is a hot-topic. If the global temperatures rises the atmosphere can contain more water vapor and more extreme weather is expected (Lenderink and van Meijgaard, 2008), and more floods are expected because of more extreme precipitation. On a short timescale it is possible to do accurate prediction nowadays, because of improved computer models and computational power. On the longer timescales however, the uncertainty of the prediction is very large. But even when predicting the weather forecast on shorter timescales there is still room for improvement in the models that are used.
As shown by Dufresne and Bony (2008) the largest uncertainty in climate models is caused by clouds, see figure 1.1. Part of this problem is caused by the fact that shallow boundary layer clouds are smaller than a single gridbox of the climate model. Since this gridbox is the smallest size that the model can actually resolve, a method is needed to account for the influence of these clouds on the resolved part of the simulation. This is called parametrizing, and this parametrization is thus very important for the dynamics of the model and any prediction the model tries to make.

This report focuses on a small aspect of the climate, namely shallow cumulus convection. Even this specific type of weather has many aspects that are not fully understood, even if this might be considered as one of the more simpler cumulus cloud-cases since the precipitation is small to none. Even though these clouds are small, their presence is very important for the transport of heat and moisture into the higher layers of the atmosphere because they occur frequently and usually in large groups. The clouds also interact with the incoming solar radiation and the outgoing radiation from the ground, some radiation is reflected and some is absorbed.
A method that is used to study these problems is with a Largy-Eddy Simulation (LES). This technique is employing a resolution that is a lot higher than a typical weather forecast model or a climate model, in the order of tens meters. This means that the resolution is high enough to resolve most of the clouds, although the eddies smaller than the gridboxes still need to be parametrized. Running a LES is computationally very ex-

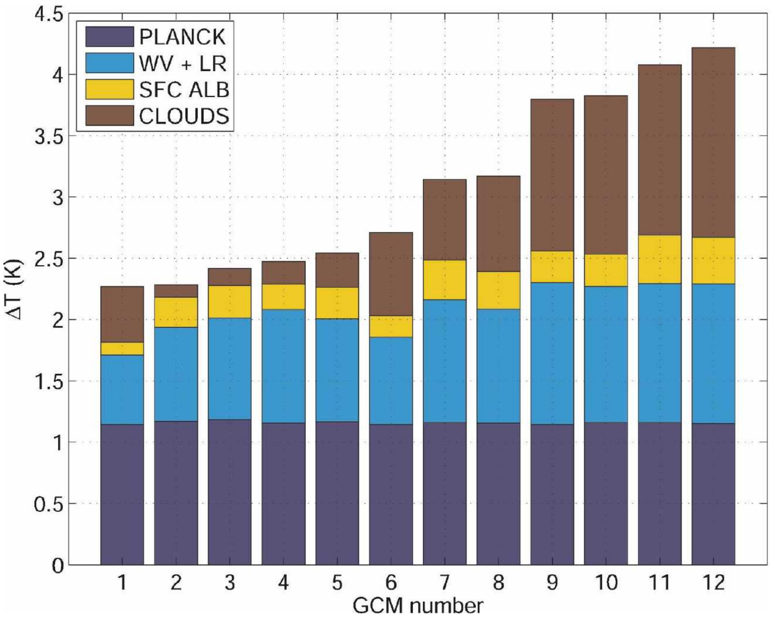

Figure 1.1: Global temperature change due to different feedback mechanisms for 12 general circulation models. The purple bars stand for the radiation effects, blue for the water vapor feedback, yellow for the surface albedo feedback and brown is the feedback due to clouds. The models are placed in order of temperature change, courtesy of Dufresne and Bony (2008).

pensive compared to a weather forecast or a climate model, but fortunately computers have become powerful enough recently to run a LES on a relatively large domain (a few kilometers by a few kilometers, with still a decent resolution) in an acceptable amount of time.

The resolution of the LES model is such that the largest eddies of a three-dimensional turbulent field are explicitly resolved, because the large eddies depend on the explicit geometry of the problem. The smaller eddies and turbulent transport are parametrized (Siebesma, 1998), according to the principle that small eddies have a universal character. This principle is shown in equation 1.1.

$$(\frac{\partial\overline{\phi}}{\partial t}) = (\frac{\partial\overline{\phi}}{\partial t})_{resolved} + (\frac{\partial\overline{\phi}}{\partial t})_{parametrized} \tag{1.1}$$

Where ϕ denotes an arbitrary dynamic variable, and the overbar denotes the horizontal (spatial) average. This means that the grid can be more coarse than with a Direct Numerical Simulation (DNS), so that computational effort is reduced.

1.2 BOMEX and basics of cumulus clouds

The case that is used throughout this report is the Barbados Oceanopgrahic and Meteorological Experiment (BOMEX) case. The profiles of some of the thermodynamic variables of BOMEX are shown in figure 1.3. It is a shallow cumulus convection case, which means that only shallow (as in, non-precipitating) cumulus clouds form. The clouds studied in this report are over the sea, but in nature these clouds also occur above lands frequently.

Figure 1.2: Shallow cumulus clouds, the picture was taken during the AMMA field campaign from an aircraft flying over Niger. As can be noted from the picture the individual clouds are not very large but as a group the cloud cover is around 10%

The surface emits moisture and heat into the atmosphere, and because of this organised structures containing thermals form. These thermals reach up to 500 meters height, where they become negatively buoyant. If a thermal generates enough vertical velocity to reach higher into the atmosphere then the temperature in the thermal is decreasing enough so that the moisture in the thermal starts to condensate. This condensation releases heat which acts as a mechanism for the cloud to rise further in the atmosphere. Some clouds are small and reach a cloud depth of only a few hundreds of meters, but some cloud have enough energy to grow to about 1500m, where an inversion is present. This inversion is a layer of warmer air on top of the layer where the cloud form, and this basically acts as a lid on top of the jar. The strongest clouds may penetrate for some distance into the inversion, but the inversion is in the case of shallow cumulus clouds strong enough to stop these clouds, so no deep convection occurs. Around a cumulus cloud a subsiding shell is present, this shell compensates for the upward motion in the core of the cloud. This shell exists because the cloudy air that is leaving the cloud (detrainment) is mixing with environmental air. This mixture of air is drier than the cloudy air, so the liquid water in the mixture evaporates, which leads to cooling. This cooling removes heat, and thus buoyancy, from this mixture, so that it starts to descend.

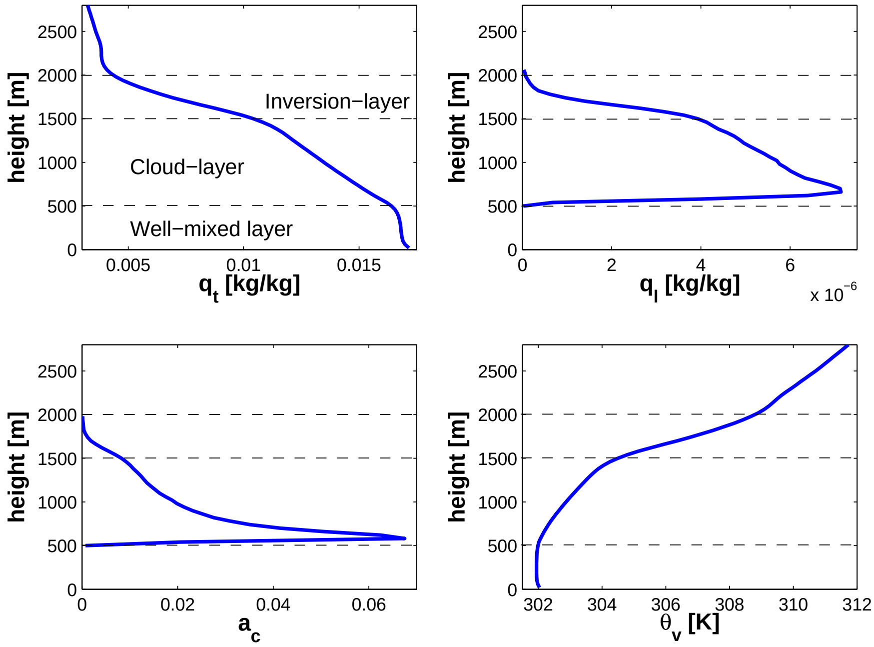

Figure 1.3: Vertical profiles for the total specific humidity (top left), the liquid water specific humidity (top right), the cloud fraction (bottom left) and the virtual potential temperature (bottom right).

The profiles in figure 1.3 are obtained from a LES simulation and are horizontally averaged in space and time-averaged over one hour. As can be seen the cloudbase is around 500m (because at this point liquid water starts to form) and the cloud tops are near 1500m. An inversion is visible at 1500m, which explains the clouds ending there. The case is (after the spin-up time) in a steady-state, which means that it is an ideal case to use for a parameter study, since any change in the behaviour is due to the change of the parameter, and not due to a change in time.

1.3 Scale dependence

Up till the recent past, weather forecast models used a horizontal resolution of 28∼55km (ECMWF, 2007), which means that the resolution is too coarse to resolve any turbulent eddies explicitly. The turbulent transport is determined through parametrization, using an ensemble approach. The ensemble approach uses the fact that the gridbox is large enough that the average cloud properties in each gridbox are similar. Because of the fast increase of computing power (Moore's Law states that computing power doubles every 18 months) the weather forecast models now run with smaller grid sizes (∼2km). This means that some eddies might be explicitly resolved, so these eddies do not need to be parametrized anymore. The influence of these smaller grid sizes on the accuracy of the forecast are investigated in this report, especially how the parametrization behaves. The problem is illustrated in figure 1.4.

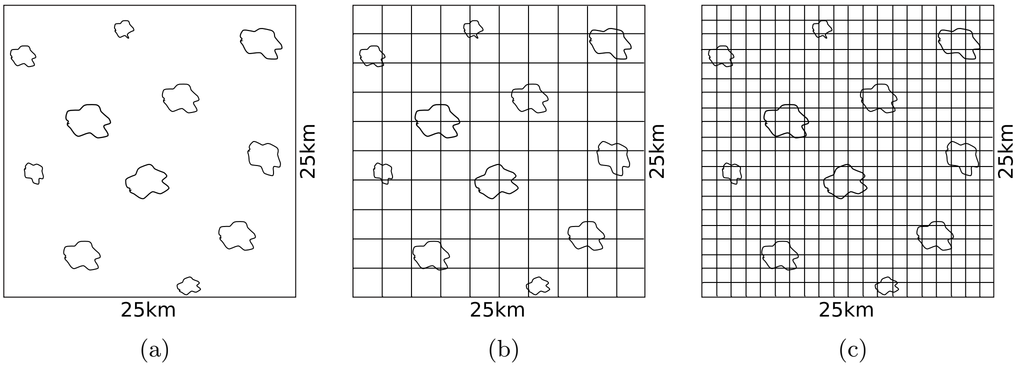

Figure 1.4: Schematic illustration of the scales of different models. On the left one gridbox of a weather forecast model is shown with a dimension of 25×25km. In the middle a resolution is shown that the model is using now, 2.5×2.5km. On the right a Large-Eddy Model is shown schemetically, the real resolution of a Large-Eddy Model is in the order of tens of meters.

The figure in the left panel of figure 1.4 (a) shows one gridbox of the weather forecast model that was used until recently. Multiple clouds are present in one gridbox, so that the ensemble approach is valid. Because of the higher resolution, the current situation is the one depicted in (b). The gridboxes are still larger than the largest turbulent eddies, but the average properties of the gridboxes are no longer similar for all the gridboxes. This means that the parametrization of the turbulent eddies that is used until now could no longer be valid. For comparison the method (LES) that is used in this report to investigate this problem is shown in panel (c). The gridboxes are small enough to resolve most of the turbulent eddies, so a LES can be used as a virtual laboratorium.

1.4 General behaviour of the system

As can be seen in the schematic figure 1.4, the eddies on the scales that are smaller than the gridsize are not calculated explicitly, but need to be parametrized since these are smaller than the gridboxes of the model. For the case of shallow cumulus, the parametrization of the turbulent transport is especially important since almost all the clouds are smaller than the gridboxes. As was mentioned in section 1.1, the clouds are very important for the thermodynamics of the system, and thus the parametrization of the subgrid turbulent eddies is important. This part of the research does not look at the resolution dependence of the parametrization, but at how the parametrization behaves on a larger scale when the standard shallow cumulus case is perturbed in various ways. These perturbations are simply done by perturbing the initial state of the system at the startup of the simulation. After perturbing the system, the effect of these perturbations on the mean state is also analyzed. The mean state of the system can be quantified through different concepts which are explained in chapter 3.

1.5 Outline

This report focuses on two aspects of shallow cumulus convection: the first is the behaviour of the system when the resolution of the weather forecast or climate model changes, since this causes changes in each individual gridbox. The second aspect is the behaviour of shallow cumulus convection is general. Relationships between the parametrization of the turbulent eddies (chapter 2), mean state of the system (explained in chapter 3) and perturbations to the system are examined. Chapter 2 also explains some basic thermodynamics, statistics and sampling methods that are used throughout the report. In chapters 4 and chapter 5 the results for the analysis of the two aspects are presented. This report then finishes with conclusions and recommendations for future work.

Chapter 2

General methods and parametrization

In this chapter some concepts are explained that are used for this research. In 2.1 some basic thermodynamics are explained. After that the definitions of some statistical quantities that are used throughout this report are given in section 2.2. The simulation that is used during this research is the Dutch Atmospheric Large-Eddy Simulation (DALES), basic information about the way information is obtained from the simulation is presented in section 2.3. After that the first part of the research is discussed in section 2.5.

2.1 Thermodynamics

In cloud physics one often works with parcels of airs, and it is convenient if a mixture of two parcels can be described by a linear combination of the properties of the two individual parcels. This is possible if the internal sources and sinks are eliminated, and to this end 'conserved' variables are introduced. The method to calculate some on these conserved variables is explained in this section. Section 2.1.1 gives the definitions for the conserved variables used in this report and describes how the virtual potential temperature is calculated. Section 2.1.2 gives a definition for the mass flux.

2.1.1 Calculating the virtual potential temperature

The conserved variables for moisture and heat are given by (Siebesma, 1998)

$$q_t = q_v + q_l \tag{2.1}$$

$$\theta_l = \theta - \frac{L_v}{C_p} \cdot \frac{1}{\pi} \cdot q_l \tag{2.2}$$

where q_v is the water vapor specific humidity, q_l the liquid water specific humidity and q_t the total specific humidity. The specific humidity is the ratio of the mass of water to the total mass of dry air and water. q_t is a conserved variable since the only sinks and sources (condensational effects) are in q_v and q_l when no precipitation is present. In equation (2.2) the L_v stands for the latent heat of evaporation and C_p is the specific heat capacity at constant pressure for dry air. The values for these constants can be found in appendix A. θ is the potential temperature which is linked to the temperature

T by the Exner function π

$$\theta = T\pi^{-1} \tag{2.3}$$

$$\pi = (\frac{p}{p_0})^{\frac{R_d}{C_p}} \tag{2.4}$$

where p is the average pressure at a certain height, p_0 is the reference pressure and R_d is the gas costant for dry air. The potential temperature is the temperature a parcel would have if the parcel is compressed or expanded adiabatically to a pressure p_0. The potential temperature is a conserved variable for dry (no phase changes) adiabatic processes. Since cloud physics involves phase changes, the liquid water potential temperature θ_l is a more convenient variable since it is conserved for moist adiabatic processes.
The virtual potential temperature θ_v is the potential temperature that the air would have if the air were completely dry (completely free of water). The formula for θ_v is given by (de Roode, 2004)

$$\theta_v = \theta \cdot (1 + \lambda q_v - q_l) \tag{2.5}$$

where λ is a constant given by

$$\lambda = \frac{R_v}{R_d} - 1 \approx 0.608 \tag{2.6}$$

where R_v is the specific gas constant for moist air and R_d is the specific gas constant for dry air. By using (2.4) to determine π and plugging this into (2.2), θ can be calculated. This result can then be used to calculate θ_v by using (2.5).The virtual potential temperature is also closely related to the buoyancy by

$$B = \frac{g}{\theta_0}(\theta_v - \overline{\theta_v}) \tag{2.7}$$

where B is the buoyancy and θ_0 is a reference temperature.

2.1.2 Mass flux

An important variable in the parametrization of moist convection is the mass flux in the cloud core. This mass flux is defined as (Siebesma, 1998)

$$M = \rho\sigma(w_c - \overline{w}) \tag{2.8}$$

Where ρ is the density, σ is the cloud fraction, $\overline{w}$ is the average vertical wind velocity averaged over the horizontal domain and w_c is the vertical velocity sampled in the cloud or cloud core, depending on the sample criterium (see section 2.5.3 for more information). Often the average vertical wind velocity $\overline{w}$ is assumed to be much smaller than w_c which leads to

$$M \approx \rho\sigma w_c \tag{2.9}$$

2.1.3 Relative humidity

Another variable that is often used is the relative humidity. The relative humidity is important because it can be seen as a 'cutoff' humidity at which clouds start to form. The formal definition of the RH is given by (Bohren and Albrecht, 1998)

$$RH = \frac{e}{e_s} \tag{2.10}$$

where e is the water vapor pressure and e_s is the saturation vapor pressure. The water vapor pressure follows from the gas law

$$e = \rho_v R_v T \tag{2.11}$$

where ρ_v is the density of water vapor. The saturation vapor pressure follows from the Clausius-Clapeyron equation

$$\frac{de_s}{dT} = \frac{1}{T}\frac{L_v}{v_v - v_l} \tag{2.12}$$

the derivation of this equation can be found in de Roode (2004). In this equation v_v stands for the specific volume of water vapor and v_l is the specific volume of liquid water. Using the approximation from Stull (1988) for typical temperatures in the atmospheric boundary layer the following form for e_s is obtained

$$e_s = 610.78 \exp(\frac{17.2694(T - 273.16)}{T - 35.86}) \tag{2.13}$$

with the temperature T in units Kelvin. The relative humidity defined in equation (2.10) can also be written in terms of specific humidities, this is more convenient since the LES output contains the specific humidity. Using the following equation from Bohren and Albrecht (1998) for the relationship between the mixing ratio and the vapor pressure:

$$\frac{r}{r_s} = \frac{e}{e_s}(\frac{p - e_s}{p - e}) \tag{2.14}$$

And realising that $e << p$ and that $e_s << p$ (e and e_s are both the same order of magnitude) gives the following simplified equation

$$\frac{r}{r_s} = \frac{e}{e_s} \tag{2.15}$$

So the equation for the relative humidity can be rewritten as

$$RH = \frac{r}{r_s} \tag{2.16}$$

The mixing fraction and the saturation mixing fraction is related to the specific humidity and the saturation specific humidity in the following way (Bohren and Albrecht, 1998)

$$q = \frac{r}{1 + r} \tag{2.17}$$

$$q_{sat} = \frac{r_s}{1 + r_s} \tag{2.18}$$

The same reasoning holds for q so these specific humidities can be used to define the relative humidity in another way by diving equation (2.17) by equation (2.18) and by realising that r is very small in the atmosphere (<<1) so that $q_{sat} \approx r_s$, which gives

$$RH \approx \frac{q_t}{q_{sat}} \tag{2.19}$$

Which is the definition that is used in the remainder of this report.

2.2 Statistical toolbox

When statistically analysing data a few concepts are important. First a definition is given for different types of averaging in section 2.2.1. After that the variance and standard deviation of a variable are discussed in section 2.2.2.

2.2.1 Averaging

Two types of averaging are often used in this report, and therefore it is important to define what type of averaging is used in a certain situation. The first type is a spatial average, which in our case means the average of a certain variable ϕ over an entire horizontal slab. This average is defined as

$$\overline{\phi} = \frac{1}{A}\int_0^{L_x}\int_0^{L_y}\phi dxdy \tag{2.20}$$

Where A is the surface of the horizontal slab and L_x and L_y are the sizes of the slab in the x- and y- dimensions. This equation is discretized so it can be used with the LES

$$\overline{\phi}(k;n) = \frac{1}{N_x N_y}\sum_{i=1}^{N_x}\sum_{j=1}^{N_y}\phi(i,j,k;n) \tag{2.21}$$

In (2.21) N_x stands for the number of grid points in the x-direction and N_y stands for the number of grid points in the y-direction. The variables i, j, k are used to give the spatial position of a gridbox in the x, y, z space and n is an indicator for the current timestep.

Apart from the (spatial) slab average, time averages are also used. The simulation has a running time of a certain timespan, and during this time the variables are stored in output files at certain times. The instantaneous variables at these times can be averaged over a timespan by

$$< \phi >= \frac{1}{T}\int_0^{T}\phi dt \tag{2.22}$$

where T stands for the total averaging time. Equation (2.22) can be discretized as

$$< \phi(i,j,k) >= \frac{1}{N_t}\sum_{n=1}^{N_t}\phi(i,j,k;n) \tag{2.23}$$

where N_t is the total number of timesteps over which the averaging takes place.

2.2.2 Variance and standard deviation

The fluctuations of a variable ϕ are (Jonker, 2008)

$$\phi'(i,j,k;n) = \phi(i,j,k;n) - \overline{\phi}(k;n) \tag{2.24}$$

Where $\overline{\phi}$ is the horizontal average of the variable, given by equation (2.21). Equation (2.24) can then be used to define the instantaneous variance profile (Jonker, 2008)

$$\overline{\phi'^2}(k;n) = \frac{1}{N_x N_y}\sum_{i=1}^{N_x}\sum_{j=1}^{N_y}\overline{\phi'}^2(i,j,k;n) \tag{2.25}$$

The variance is a measure of the statistical dispersion of a variable, and is used to give an estimate for the spread of that variable.

Another way of looking at the spread of a variable is the standard deviation. The standard deviation is expressed in the same units as the original variable, whereas the unit of the variance is the square of the unit of the original variable. To estimate the standard deviation of a variable the following definition is used

$$\sigma = \sqrt{\overline{\phi'^2}} \tag{2.26}$$

2.3 Dutch Atmospheric Large-Eddy Model

A LES model is used when the computational power at hand is not large enough to solve the fluid mechanics equations directly. To directly compute all the eddies from the smallest ($\approx$ 10 mm) to the largest scales ($\approx$ 1 km) would require $\approx 10^{18}$ gridpoints. That is why a LES is used since a LES is able to resolve the large eddies explicitly while the effects of the eddies smaller than the gridbox size are parametrized. This method works very well since these large eddies of $\approx$ 1 km in the atmosphere are accounting for the bulk of the transport for shallow cumulus clouds. Furthermore the large eddies depend on the geometry and stratification of the environment, while the behaviour of the smaller eddies is statistically similar in turbulent flows. In this report the specific LES model that is used is the Dutch Atmospheric Large-Eddy Model, DALES. This model has been developed for many years, and is used in this research as a 'virtual laboratory'. This means that the output of the model is treated as a large series of measurements, and that these measurements can be used to investigate the problems at hand. Before briefly giving some information about the output of the LES in section 2.3.2, the basic governing equations in the model are given in section 2.3.1. For more detailed information about the equations and the closure of the subgrid model the reader is referred to Deardorff (1973), Heus (2008) and van Zanten (2000).

2.3.1 Governing equations

Three conserved variables are governing the LES equations in DALES: momentum, energy and mass. The conservation of momentum is given by the Navier-Stokes equations, the conservation of energy is written in terms of the conserved variables q_t and θ_l and the conservation of mass is given by the continuity equation.
The three general Navier-Stokes equations are given by (Kundu and Cohen, 2008)

$$\rho\left(\frac{\partial u_i}{\partial t} + \frac{\partial u_j u_i}{\partial x_j}\right) = -\frac{\partial p}{\partial x_i} + \frac{\partial}{\partial x_j}\left(\mu \frac{\partial u_i}{\partial x_j}\right) + F_{ijk} \tag{2.27}$$

where the subscript j is used as an implicit sum, x_j is the cartasian coordinates (x, y, z), u_j is the velocity in the (u_x, u_y, u_z) direction, μ is the viscosity and F_{ijk} represents the body forces. The subscript i is used to distinguish between the three equations.

The external forces are gravity and coriolis forces. Using the Boussinesq approximation (ignoring density variations except in the gravitational term) and ignoring the viscosity since it is many times smaller than the other terms, the filtered (Deardorff, 1973) LES equation (2.27) is rewritten as (van Zanten, 2000) (for readability, all tildes are omitted on the filtered variables)

$$\frac{\partial u_i}{\partial t} = \frac{g}{\theta_0}(\theta_v - \overline{\theta_v})\delta_{i3} - \frac{\partial u_j u_i}{\partial x_j} - \frac{\partial \pi}{\partial x_i} - \frac{\partial \tau_{ij}}{\partial x_j} - 2\varepsilon_{ijk}\Omega\eta_j u_k \tag{2.28}$$

where δ_{ij} is the Kronecker delta, ε_{ijk} the alternating unit tensor, Ω is the earth's angular velocity, η_j is the jth component of a unit vector parallel to the axis of rotation ($\eta_j \in (0,\cos\phi,\sin\phi)$ where ϕ is the latitude) and π is the modified pressure term (van Zanten, 2000).
Conservation equations for q_t and θ_l are given by (van Zanten, 2000)

$$\frac{\partial \psi}{\partial t} = -\frac{\partial u_j \psi}{\partial x_j} - \frac{\partial \overline{u_j'' \psi''}}{\partial x_j} + S_\psi \tag{2.29}$$

where ψ can be either q_t or θ_l, $\overline{u_j'' \psi''}$ stands for the subgrid flux terms and S_ψ stands for the source/sink term which, for shallow boundary layers, incorporates the processes precipitation and radiation.

The parametrizations for subgrid terms from equation (2.28) and equation (2.29) are given by (van Zanten, 2000)

$$\overline{u_j'' \psi''} = -K_\psi \frac{\partial \psi}{\partial x_j} \tag{2.30}$$

$$\tau_{ij} = -K_m \left(\frac{\partial u_i}{\partial x_j} + \frac{\partial u_j}{\partial x_i} \right) \tag{2.31}$$

where K_ψ is the eddy diffusivity and K_m is the eddy viscosity, with again $\psi \in q_t, \theta_l$. K_ψ and K_m are a function of the turbulent kinetic energy e, which is evaluated using

$$\frac{\partial e}{\partial t} = -u_j \frac{\partial e}{\partial x_j} - \tau_{ij} \frac{\partial u_i}{\partial x_j} + \frac{g}{\theta_0} \overline{w'' \theta_v''} - \frac{\partial \overline{w'' e''}}{\partial x_j} - \frac{1}{\rho_0} \frac{\partial \overline{w'' p''}}{\partial x_j} - \epsilon \tag{2.32}$$

which is the prognostic equation for the subgrid turbulent kinetic energy e. For more information about how to calculate all the terms from equation (2.32) see Heus (2008).
Finally the conservation of mass is given by the continuity equation for an incompressible flow

$$\frac{\partial u}{\partial x} + \frac{\partial v}{\partial y} + \frac{\partial w}{\partial z} = 0 \tag{2.33}$$

2.3.2 Model output

The model produces two types of output that are used for analysis. The first type of output contains variables that are averaged both in space and time. The variables are horizontally averaged in space and then these variables are sampled every 12 seconds for a total time of 600 seconds. Then this collection of time samples is time-averaged and the results are written to disk in simple textfiles. Since this does not generate a lot of data (only a small piece of text every 600 seconds) this method is very convenient to use on all variables available. Any results in this report that are not dependent on the subdomain decomposition are obtained using this method.

The second type of output consists of the entire 3D field of various variables. These are instantenous fields, which basically means it is a snapshot of the simulation at a certain time. Since a lot of data is generated this way, the instantaneous fields are only written to disk once every 10 minutes. This means that the 3D fields contain a lot of spatial information (since the value of the variable in every gridbox is known), but there is not a lot of information about the time evolution. This means that the results for the subdomain decomposition have bad time statistics because the entire 3D field is needed. To further reduce the amount of data that is produced by the simulation, not all available variables are saved in this way. Only the following variables are in the 3D output files from the simulation: liquid water potential temperature (θ_l), total water specific humidity (q_t), the liquid water specific humidity (q_l) and the wind velocity components u,v,w. As an example, the virtual potential temperature (θ_v) thus needs to be calculated from these output variables, this is discussed in section 2.1.1.

2.4 BOMEX input profiles

In this section the details about the BOMEX standard input profiles and large scale forcings are given. This information is all the information that is needed as input for the LES model to simulate shallow cumulus convection.

2.4.1 Initial profiles

The input profiles for u, v, q_t and θ_l are given in tables 2.1 to 2.3. Other variables can be calculated from these input profiles assuming hydrostatic equilibrium. Initially ($t = 0$), it is assumed (Siebesma, 1997) that there is zero liquid water (q_l =0), so that:

$$\theta = \theta_l \tag{2.34}$$

$$q_v = q_t \tag{2.35}$$

During the startup phase of the simulation, the clouds start to form and after about three hours the simulation (almost) is in a steady state.

Table 2.1: Information about the initial profile for u.

Height[m]	u[m/s]
0 - 700	-8.75
> 700	-8.75 + 1.8×10^{-3} (z - 700)

The velocity component v is set to 0 m/s on every height initially.

Table 2.2: Information about the initial profile for the total specific humidity.

Height[m]	q_t[g/kg]
0 - 520	17.0 + (16.3 - 17.0)/(520) × z
520 - 1480	16.3 + (10.7 - 16.3)/(1480 - 520) × (z - 520)
1480 - 2000	10.7 + (4.2 - 10.7) /(2000 - 1480) × (z - 1480)
> 2000	4.2 - 1.2×10^{-3}(z - 2000)

The input profiles for q_t and θ_l are chosen in such a way (based on observations) that an inversion starts at 1480m up to 2000m.

Table 2.3: Information about the initial profile for the liquid water potential temperature.

Height[m]	θ_l[K]
0 - 520	298.7
520 - 1480	298.7 + (302.4 - 298.7)/(1480 - 520) × (z - 520)
1480 - 2000	302.4 + (308.2 - 302.4)/(2000 - 1480) × (z - 1480)
> 2000	308.2 + 3.65×10^{-3} (z - 2000)

2.4.2 Large scale forcings

The large scale forcings are listed in table 2.4 to 2.6. The subsidence is applied on the prognostic fields q_t, θ_l, u and v.

Table 2.4: Information about the large scale subsidence.

Height[m]	w[m/s]
0 - 1500	- (0.0065/1500) × z
1500 - 2100	- 0.0065 + 0.0065/(2100 - 1500) × (z - 1500)
> 2000	0

The subsidence between 1500 and 2100 meters is chosen in such a way that it keeps the inversion at the same height.

Table 2.5: Information about the radiative cooling.

Height[m]	$\frac{d\theta}{dt}$[m/s]
0 - 1500	-2.315 ×10^{-5}
1500 - 2500	-2.315 ×10^{-5} + 2.315 ×10^{-5} /(2500 - 1500) × (z - 1500)
> 2500	0

The radiative cooling is lower in the inversion layer than in the cloud layer, because the clouds induce a radiative cooling term.

Table 2.6: Information about the large scale horizontal advection.

Height[m]	$\frac{dq_t}{dt}$[kg/kg/s]
0 - 300	-1.2 ×10^{-8}
300 - 500	-(1.2 ×10^{-8} - 1.2×10^{-8} (z-300)/(500-300))
> 500	0

The only significant diagnosed large scale advection term is a low level drying of about 1 g/kg/day. All other large scale advection terms are set to zero.

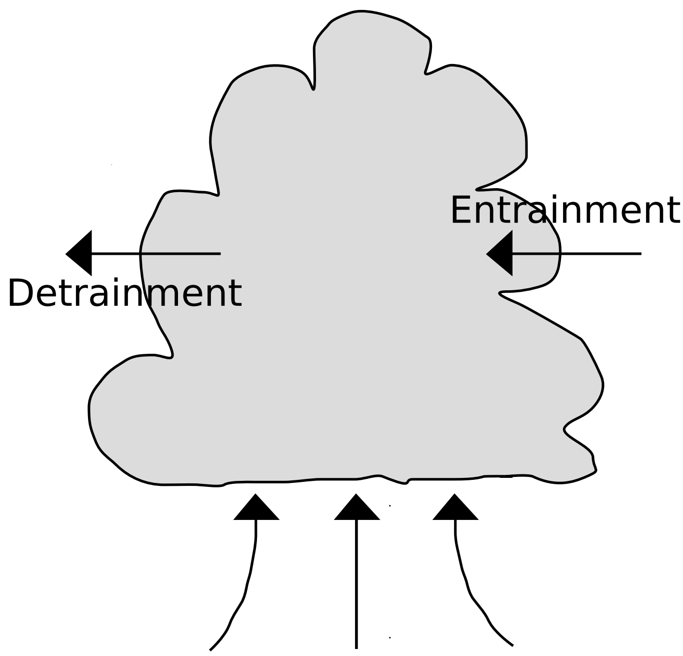

Figure 2.1: A schematic view of the entrainment and detrainment.

2.4.3 Surface conditions

Two methods to prescribe surface conditions are used in this report. This first method is to prescribe the kinetic moisture flux $(\overline{w'q'})_S$ and the kinetic temperature flux $(\overline{w'T'})_S$. The second method is to keep the liquid water potential temperature fixed at a constant value at the surface (θ_l) and let the LES choose the surface fluxes based on this temperature. In the standard BOMEX case the surface fluxes are prescribed, so in this report this method is used unless mentioned otherwise.

Table 2.7: The conditions prescribed at the surface of the LES for the two methods mentioned.

Method	$\overline{w'q'}$[kg kg^{-1} m s^{-1}]	$\overline{w'T'}$[K m s^{-1}]	θ_l[K]	surface pressure [mB]
1	8e-3	5.2e-5	-	1015
2	-	-	299.1	1015

2.5 Entrainment and detrainment

Clouds mix with the environment. The flow of environmental (dry) air into the cloud is called the entrainment. The process of air flowing out of the cloud into the environment is called the detrainment, a schematic overview is given in figure 2.1. The dynamics of clouds and the environment are heavily dependent on this mixing process, therefore it is important that a model has a good method to deal with this ongoing entrainment and detrainment process. Since these processes are subgrid processes, a weather forecast or climate model is not able to calculate the entrainment and detrainment values for each cloud. Therefore, the entrainment and detrainment need to be parametrized. An overview is given of the way this parametrization takes place in a large-scale model in section 2.5.1. In section 2.5.2 it is explained how the entrainment and detrainment rates can be diagnosed from the simulation results after the simulation is finished. Since entrainment and detrainment represent the mixing process of clouds and environment, a way is needed to distinguish between clouds and environment. The sampling criteria to find clouds are therefore also discussed.

2.5.1 Modelling in a large-scale model

The method that is currently used in the model to parameterize the entrainment and detrainment is called the mass-flux approximation. This method is described in Siebesma (1998), but a short review is presented here. The starting point of the derivation is the spatially averaged continuity equation for a cloud core as presented in Siebesma (1998)

$$\frac{\partial a_c}{\partial t} + (D - E) + \frac{\partial a_c w_c}{\partial z} = 0 \tag{2.36}$$

Where a_c is the cloud core fraction and D, E are the lateral detrainment and entrainment rates given by

$$D - E = \frac{1}{A} \oint_{Interface} \hat{n} \cdot (\vec{u} - \vec{u}_i) dl \tag{2.37}$$

A is the area of the interface, $\hat{n}$ is the unit vector perpendicular to the surface, $\vec{u}$ is the 3D velocity vector of the mass flow at the surface and $\vec{u}_i$ is the velocity of the surface. This means that (2.37) only is nonzero if there is mass exchange across the surface, if the cloud is advected then this advection does not contribute to D and E.

Now we want to use the above concept in the budgets equations for an arbitrary variable. The budget equation for any variable ϕ for the cloudcore , as taken from Siebesma (1998), is as follows

$$\begin{aligned} \frac{\partial a_c \phi_c}{\partial t} &= -\frac{\partial a_c \overline{w\phi}^c}{\partial z} + a_c F_c - \frac{1}{A} \oint_{Interface} \hat{n} \cdot (\vec{u} - \vec{u}_i) \phi dl \\ \frac{\partial (1 - a_c) \phi_e}{\partial t} &= -\frac{\partial (1 - a_c) \overline{w\phi}^e}{\partial z} + (1 - a_c) F_e + \frac{1}{A} \oint_{Interface} \hat{n} \cdot (\vec{u} - \vec{u}_i) \phi dl \end{aligned} \tag{2.38}$$

The subscript c means that the variable is taken from the core of a cloud, the sampling criterion is explained in section 2.5.3. Where all source and sink terms have been incorporated into F. The idea is to make the approximation that during transport between cloud core and environment, average properties are transported. So the entrainment transports average environmental properties into the cloud core, and the detrainment transports average cloud core properties into the environment. First we need separate equations for E and D

$$\begin{aligned} E_\phi \phi_e &\simeq -\frac{1}{A} \oint_{\hat{n} \cdot (\vec{u} - \vec{u}_i) < 0} \hat{n} \cdot (\vec{u} - \vec{u}_i) \phi dl \\ D_\phi \phi_c &\simeq \frac{1}{A} \oint_{\hat{n} \cdot (\vec{u} - \vec{u}_i) > 0} \hat{n} \cdot (\vec{u} - \vec{u}_i) \phi dl \end{aligned} \tag{2.39}$$

which just defines the entrainment as the mass that flows into the cloud core, and the detrainment as the mass that flows out of the cloud. The ϕ subscripts for E and D denote a possible dependence on ϕ of these variables. Assuming that E and D do not depend on ϕ (Siebesma, 1998), we can use (2.39) to write (2.38) as

$$\frac{\partial a_c \phi_c}{\partial t} = -\frac{\partial a_c \overline{w\phi}^c}{\partial z} + a_c F_c + E\phi_e - D\phi_c \tag{2.40}$$

$$\frac{\partial (1-a_c)\phi_e}{\partial t} = -\frac{\partial (1-a_c)\overline{w\phi}^e}{\partial z} + (1-a_c)F_e - E\phi_e + D\phi_c \tag{2.41}$$

To make the final step towards the actual parametrization some other assumptions are made:

- Assume steady state in the cloud core, so that the left-hand side in (2.40) is zero
- Since the cloud core cover is much smaller than 1, we can write $\phi_e \approx \phi$
- The mass flux approximation, saying that the mass flux equals the vertical velocity times the cloud fraction.

Using these assumptions, equation (2.36) can be rewritten as

$$\frac{\partial M}{\partial z} = E - D \tag{2.42}$$

and equations (2.40) and (2.41) can be rewritten as

$$\begin{aligned} \frac{\partial M\phi_c}{\partial z} &= E\overline{\phi} - D\phi_c \\ \frac{\partial \overline{\phi}}{\partial t} &= -\frac{\partial M(\phi_c - \overline{\phi})}{\partial z} + \overline{F} \end{aligned} \tag{2.43}$$

The model that is currently used is able to handle this mixing process for an ensemble of clouds on a large gridbox, but it is unclear how the model behaves if the resolution is changed. On a large gridbox the overall cloud fraction has a certain value (usually 5-10%), but this value is not necessarily correct for a smaller gridbox of the domain. As extreme examples, a small gridbox can be completely filled with clouds, or have only a very little piece of a cloud. The range in possible cloud fractions of a gridbox can thus differ greatly. Furthermore, if the resolution is higher then more and more scales are actually resolved and less needs to be parametrized. The effects of these changes are investigated with a LES in this report.

2.5.2 Diagnosing the entrainment and detrainment from the LES

In order to investigate the dependence of the entrainment of the size of the subdomains, one must be able to determine the entrainment and detrainment rates that is calculated during the LES. Equation (2.42) is combined with the simplified (assuming steady-state) prognostic equation (de Roode, 2004) for the mean quantity of a variable in the cloud core

$$0 = -\frac{\partial M_c \phi_c}{\partial z} + E\phi_e - D\phi_c \tag{2.44}$$

which gives the following equation for the fractional (or normalized) entrainment rate

$$\epsilon = \frac{E}{M_c} = -\frac{\frac{\partial \phi_c}{\partial z}}{\phi_c - \phi_e} \tag{2.45}$$

Where ϕ can be either the total water specific humidity q_t or the virtual liquid water temperature θ_l. The subscript c stands for cloud core and the e stands for environment. The criterion for cloud core sampling is explained in the next section. In this report ϵ is always calculated using q_t, sampled in the core of the cloud instead of the cloud so that the derivative in the numerator is better defined

$$\epsilon = -\frac{\frac{\partial q_{t,c}}{\partial z}}{q_{t,c} - q_{t,e}} \tag{2.46}$$

Where the environmental total water specific humidity is assumed to be equal to the mean q_t of a slab. Formally speaking this environmental term is given by

$$q_{t,e} = \frac{\overline{q}_t - a_c q_{t,c}}{1 - a_c} \tag{2.47}$$

Assuming that $a << 1$ this reduces to $q_{t,e} = \overline{q}_t$. If assuming steady-state the fractional (or normalized) detrainment rate is given by (Siebesma, 1998)

$$\delta = \epsilon - \frac{1}{m_c}\frac{\partial m_c}{\partial z} \tag{2.48}$$

where m_c is the mass flux of the cloud core. This definition however means that the detrainment rate can reach values lower than zero if the term on the far right is larger than the entrainment. This can happen if the gradient of the mass flux is very steep and positive, which is usually the case near the cloudbase. However, a few other situations exist in which the detrainment rate can be diagnosed as negative, for example near the inversion where the cloud core is not always well-defined. These latter negative values for the diagnosed entrainment are thus purely because of the way equation (2.48) is defined and do not have a physical reason. A typical value for the diagnosed entrainment in clouds for the BOMEX case is in the order $\epsilon \approx 1 \cdot 10^{-3} m^{-1}$.

2.5.3 Cloud-core sampling

As mentioned above, a distinction between the variables in the environment and in the cloud is needed to diagnose the entrainment and detrainment rates. A cloud is defined as the occurrence of liquid water, so a gridpoint that contains liquid water also contains a cloud. The conditional sampling for cloud-point therefore is

$$q_l > 0 \tag{2.49}$$

The 'core' of a cloud is defined as the part of a cloud that is buoyant with respect to the environment. The condition that thus needs to be satisfied is that the amount of liquid water must be greater than zero and that the points must be positively buoyant

$$q_l > 0 \quad \& \quad \theta_v > \overline{\theta}_v \tag{2.50}$$

Sometimes an even stronger condition is used, which states that the cloud core is not only positively buoyant, but also has a vertical velocity that is greater than zero and thus moving upward. This is called the cloud core updraft. The sampling condition is then given by

$$q_l > 0 \quad \& \quad \theta_v > \overline{\theta}_v \quad \& \quad w > 0 \tag{2.51}$$

In this report however the less strict cloud core sampling of (2.50) is used if cloud core sampling is mentioned.

2.5.4 Scalar sampling

The core sampling has a downside: it can not be used to identify thermals in the subcloud layer, since the condition that liquid water must be present can not be met. Also, using equation (2.50) without the condition that liquid water must be present does not give valid results. Because of turbulence effects the virtual potential temperature can locally be larger than the average virtual potential temperature, even though no actual thermal is present. Near the cloud tops the opposite problem exists: gridpoints that contain liquid water do not necessarily have to be part of a thermal anymore. Using equation (2.51) also has this problem with the vertical velocity, because of turbulence the vertical velocity can locally be greater than zero even though no thermal is present.

A way to identify the thermals in the subcloud layer is proposed by Couvreux et al. (2009). This conditional sampling method makes use of a passive tracer emitted at the surface and additional conditions on some thermodynamic variables. The passive tracer is emitted at the surface and has a constant radio-active decay given by (2.52).

$$\frac{\partial C}{\partial t} = -\frac{C}{\tau_0} \tag{2.52}$$

Where C is the scalar (tracer) concentration at a certain vertical level and τ_0 is the decay time of the scalar in seconds. This scalar is then used to define a sampling criterion based on the standard deviation of this scalar at a certain vertical level. This sampling criterion is given by

$$sv' > m \cdot \max(\sigma_{sv}, \sigma_{min}) \ \& \ w > 0 \tag{2.53}$$

where m is a constant, sv' stands for the tracer concentration anomaly, w is the vertical velocity and σ_{sv} is the standard deviation of the tracer, all a taken at a certain vertical level z. σ_{min} is given by

$$\sigma_{min} = 0.05 * \frac{1}{z} \int_0^z \sigma_{sv}(k) dk \tag{2.54}$$

which is a minimum threshold that is defined for the sampling, in this case a value of 5% of the average standard deviation at lower levels is taken for $m = 1$. This is done to make sure that no point is selected in a non-turbulent environment where a standard deviation still exists, as above the cloud layer. It should be noted that the factor m can simply be used to select a different percentage of the average standard deviation at lower levels, but Couvreux et al. (2009) finds that a value of $m = 1$ gives results that are in good agreement with measurements. Therefore it is decided to also use $m = 1$.

An extra term is added to the sampling criterion in (2.53) when cumulus clouds are present. In this case there is a threshold at height

$$z^{**} = z_b + \frac{z_t - z_b}{4} \tag{2.55}$$

where z_b stands for the height where the cloud base is located and z_t stands for the height where the cloud top is located. Below this height z^{**} the original criterion of (2.53) is used, and at this level and higher the criterion is expanded to also include liquid water:

$$\text{if } z > z^{**} \text{ then } sv' > m \cdot \max(\sigma_{sv}, \sigma_{min}) \text{ \& } w > 0 \text{ \& } q_l > 0 \tag{2.56}$$

This makes sure that in the cloud layer only 'cloudy' thermals are selected, and not air that is detrained from the cloud but is still making an upward motion.

This scalar sampling is tested here briefly to determine what decay time gives similar results to the cloud core sampling in the cloud layer for the BOMEX case. This sampling is then used in section 5.3.5 to identify the characteristics of the thermals below the cloudbase, and to diagnose the entrainment and detrainment using equations similar to the ones presented in section 2.5.2. The comparison of the entrainment diagnosed with the use of the scalar sampling and the entrainment diagnosed through the cloud core sampling is shown in figure 2.2.

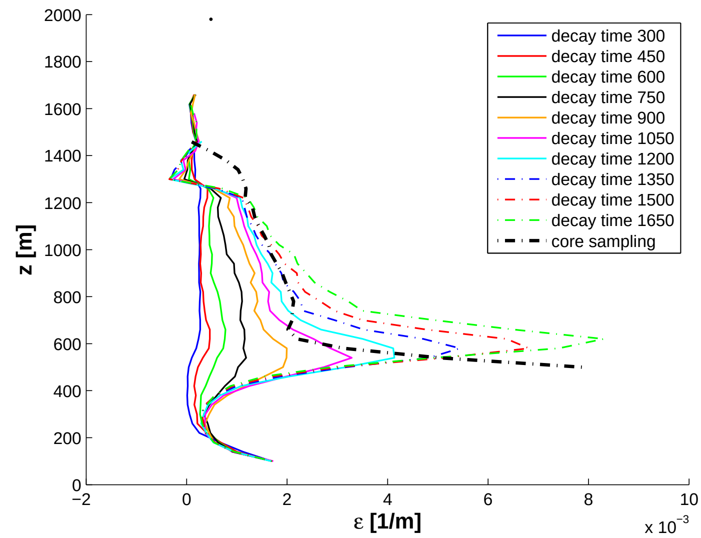

Figure 2.2: The entrainment diagnosed with the scalar sampling for different decay times compared to the entrainment diagnosed with the cloud core sampling(the black dotted line). Both are for a standard BOMEX case and averaged over the fourth hour of the simulation.

As can be seen from the figure, the shape from the diagnosed entrainment differs significant between the both types of sampling. Between 700 and 1200 meters the diagnosed entrainments do follow the same shape and have the same magnitude, and the cloud core sampling produces the same results as the scalar with a decay time of 1350 seconds. The cloud core sampling often produced bad results near the cloud base and inversion because the derivate $\frac{\partial q_{t,c}}{\partial z}$ is poorly defined. It could therefore be concluded that the scalar with a decay time of 1350 seconds is best suited for sampling the entrainment and produces better results near the cloud base and near the inversion.

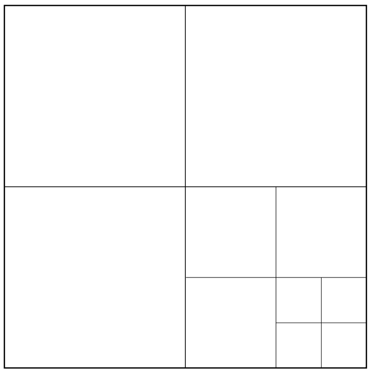

Figure 2.3: A schematic illustration of the subdomain analysis showing the dividing of the domains into subdomains. This process is repeated for every part of the full domain.

2.6 Subdomain analysis

In order to investigate the resolution dependence of the parametrization, the LES domain is divided into subdomains, which is explained in section 2.6.1 On each of these subdomains the variances of the thermodynamic variables can be calculated. This is discussed in 2.6.2. After this it is explained how the subdomains affect the calculations of the mean state variables.

2.6.1 Dividing the domain in subdomains

In order to investigate the resolution dependence of various variables, a large simulation is cut into smaller pieces (called subdomains). These subdomains can also be cut into pieces, and these pieces can be analysed, and so on. The principle is shown in figure 2.3. In principle this can be continued until the subdomain size equals the size of a single gridpoint (cell) of the simulation, but in this report the smallest subdomains usually still consist of several gridpoints. On each of these subdomains several statistical quantities can be calculated and compared with these quantities on the full domain. Since the parametrization for example is based on an ensemble-approach it is not necessarily true that a variable behaves the same on different domain sizes. On a full domain the cloud cover is approximately 10%, but on a small subdomain almost no clouds could be present, or it could be completely filled with clouds. In these examples the parametrized variables might not obey the same parametrization as on the whole domain, which is one of the goals of this research.

2.6.2 Variance scale-dependence

The scaling of the variances as the resolution of weather forecast or climate model changes is important because the entrainment and detrainment rates are closely related to the variance of q_t and θ_l. As was shown in equation (2.45), the numerator of the equation to diagnose the entrainment is given by $\phi_c - \overline{\phi}$. According to Randall et al. (1992) the variance in the mass-flux approach is given by

$$\overline{\phi'^2} = \sigma(1-\sigma)(\phi_c - \overline{\phi})^2 \tag{2.57}$$

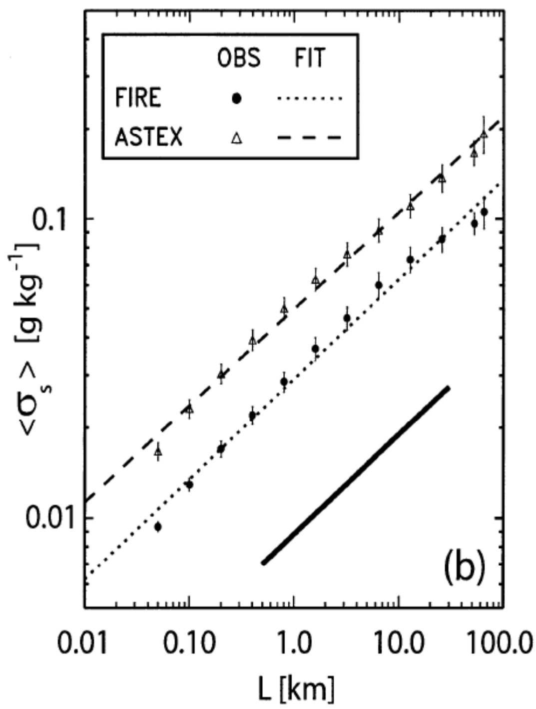

Figure 2.4: The correlation between the standard deviation of s and the size of the domain, courtesy of Wood et al. (2002).

which contains the same term as the numerator of the equation to calculate the entrainment. So if the variance changes this term might also change, which means that the entrainment also changes. So this means that a dependence of the variance on the resolution of the model is related to a change of the entrainment. Furthermore, the turbulent flux that is parametrized on the subgrid scales is also related to the variance. The Reynolds-averaged flux for shallow cumulus convection is given by (de Roode, 2004)

$$\overline{w'\phi'} = M_c(\phi_c - \overline{\phi}) \tag{2.58}$$

Again the term $(\phi_c - \overline{\phi})$ is visible, which is related to the variance. So this means that the flux is also related to the variance.

From literature on stratocumulus it is known that the standard deviation of the humidity saturation deficit (a measure of the difference between the actual thermodynamic state and the saturation curve) depends on the size of the domain (Wood et al., 2002). Wood et al. (2002) shows that this correlation follows from airplane measurements in stratocumulus clouds for two cases: ASTEX (Albrecht et al., 1995) and FIRE (Albrecht et al., 1988). This correlation is illustrated in figure 2.4. In this figure the saturation excess s is given by

$$s = q_t - q_{sat} \tag{2.59}$$

but Wood et al. (2002) defines s with conserved variables only, given by

$$s = aq_t' - b\theta_l' + c \tag{2.60}$$

The primes indicate a deviation from the mean of that quantity. The terms a,b and c have been defined as

$$
\begin{aligned}
a &= \{1 + \frac{L_v}{c_p}(\frac{\partial q_{sat}}{\partial T})\}^{-1} \\
b &= a\frac{\overline{T}}{\overline{\theta}}(\frac{\partial q_{sat}}{\partial T})_{T=T_1} \\
c &= a(\overline{q_t} - q_{sat}(\overline{T_L}))
\end{aligned}
\tag{2.61}
$$

with

$$T_1 = T - L_v q_l / c_p \tag{2.62}$$

According to Wood et al. (2002) measurements from both stratocumulus cases exhibit similar power law scaling for the standard deviation of s

$$< \sigma_S >= \alpha_S L^{\beta_S} \tag{2.63}$$

Where α_s and β_s are constants and L is proportional to the size of a subdomain. The α_s constant seems to differ between the cases, but the β_s constant is fitted to 1/3. This value is the expected value of the exponent β_s for a variable exhibiting Kolmogorov power scaling. It is therefore suggested by Wood et al. (2002) that the variance of s follows Kolmogorov-like scaling across the scales from tens of kilometers to hundreds of meters. However, this same analyses has not yet been done with the LES (DALES) that is used in this research. Since a LES does not exactly represent measurements, a large domain FIRE LES simulation is also analysed in the same manner to verify the LES results with the results from Wood et al. (2002). To this end the definition of s from equation (2.60) is used for a fair comparison.

The main aim of this research is to investigate the scaling of cumulus cloud dynamics with resolution, not stratocumulus. The paragraph above however can be used to compare stratocumulus and cumulus results, and gives a lead on what kind of analysis is useful when researching resolution dependencies. The saturation excess s is chosen because it is known that the normalized saturation deficit $Q = s/\sigma_s$ is closely related to the cloud cover (Cuijpers and Bechtold, 1995). In large-scale models the parametrized σ_s is used to estimate Q, which is used to estimate the cloud cover. This means that σ_s is used to parametrize the cloud cover in large-scale models. So keeping the previous in mind, a LES is run on a large domain for the BOMEX (cumulus) case. This LES is then analysed in the same manner as the stratocumulus simulation (FIRE) to see how the variance of s and some thermodynamic variables scale with resolution. In chapter 4 the results for the scaling of variances for this BOMEX case are presented.

Chapter 3

Mean state variables and relative humidity sensitivity experiments

Mean state variables give an indication of the mean state of the system, and might therefore be of help when investigating the scale dependence problem. In section 3.1 the idea behind commonly used mean state variables is explained. However, the BOMEX case that is used throughout this report is known to be very stable and (almost) time-independent, which means that the mean state of the simulation does not change much. This makes it hard to investigate relations between a mean state variables and other variables. In order to get more variability in the mean state variables, the standard case is perturbed in different ways. This is discussed in section 3.3.

3.1 Mean state variables

In boundary layer physics, two mean state variables are often used. The first mean state 'variable' (which are actually two variables that are closely related) is the Convective Inhibition (CIN) and the Convective Available Potential Energy (CAPE). This measure of mean state is explained in 3.1.1. The other way to describe the mean state of the system is through the concept of the critical mixing fraction (χ_{crit}). More information about this mixing fraction can be found in section 3.1.2.

3.1.1 CIN and CAPE

To investigate how far a rising thermal will ascend, a parcel is released near the surface and then lifted adiabatically. Figure 3.1 illustrates the profile that the θ_v follows of a rising parcel. As can be noticed in this figure, there is a difference between the profile that the parcel follows and the profile of the virtual potential temperature of the environment. This difference is a measure of whether clouds can form, and it can be quantified with the Convective Inhibition (CIN) and the Convective Available Potential Energy (CAPE). The values of CIN and CAPE are thus a measure of the mean state of the system.

$$CAPE = g\int_{LFC}^{LNB} \frac{\theta_v - \overline{\theta}_v}{\overline{\theta}_v} dz \tag{3.1}$$

$$CIN = g\int_{LCL}^{LFC} \frac{\theta_v - \overline{\theta}_v}{\overline{\theta}_v} dz \tag{3.2}$$

In figure 3.1 the area between the θ_v of the parcel and the average θ_v of the environment at heights between the LCL and the LFC is defined as the CIN. The area between the θ_v of the parcel and the average θ_v of the environment at heights between LFC and LNB is defined as the CAPE.

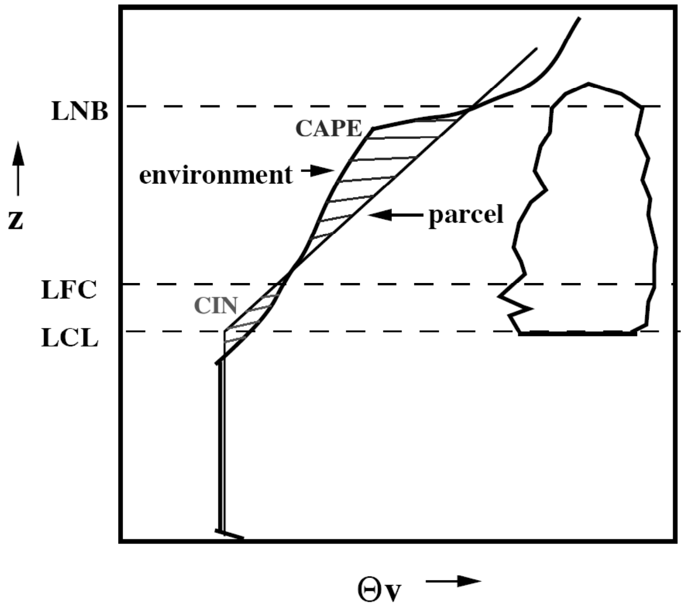

Figure 3.1: A schematic overview of the average θ_v of the environment and a parcel, courtesy of Siebesma (1998). The area between the LCL and the LFC is the CIN, the area between the LFC and the LNB is the CAPE.

Before explaining what happens to a rising parcel, some knowledge on dry and moist adiabatic lapse rates is needed. When a parcel of air is lifted adiabatically in the atmosphere it cools down. Depending on whether the parcel is saturated or not the temperature decreases at a certain rate (Siebesma, 1998). The rate at which the parcel cools down is given by the adiabatic lapse rate Γ. The dry adiabatic lapse rate is given by (3.3), the moist adiabatic lapse rate is given by (3.4).

$$\Gamma_d = -(\frac{dT}{dz})_{parcel} = -(\frac{\partial T}{\partial z})_{h_d} = \frac{g}{c_{pd}} \tag{3.3}$$

$$\Gamma_m = -(\frac{dT}{dz})_{parcel} = -(\frac{\partial T}{\partial z})_{h_l,q_t} = \frac{g}{c_{pd}} \frac{1 + \frac{L_v q_s}{R_d T}}{1 + \frac{L_v}{c_p}\frac{\partial q_s}{\partial T}} \tag{3.4}$$

Where h_d and h_l are the dry and liquid water static energy which are given by (3.5).

$$\begin{aligned} h_d &= c_{pd}T + gz \\ h_l &= c_{pd}T + gz - L_v q_l \end{aligned} \tag{3.5}$$

All other constants can be found in appendix A. The moist adiabatic lapse rate is thus always smaller than the dry adiabatic lapse rate because of the release of energy if water condensates. For detailed information on the dry and moist adiabatic lapse rate see Siebesma (1998).

In order to calculate the CIN and CAPE of a particle the θ_v profile of the parcel is needed. A parcel is raised adiabatically, which means that the total amount of water in the parcel and the liquid water potential temperature of the parcel are constant. In our case the total amount of water in the parcel (q_t) and the liquid water potential temperature (θ_l) are taken as the values of the environment at a height of 20 meter because this is the lowest available height in the LES. At this point the θ_v of the environment is slightly decreasing, which makes sure that the parcel is positively buoyant.

As the parcel rises it cools down due to expansion following the dry adiabatic lapse rate, and if the parcel rises far enough the temperature decreases such that the humidity content becomes equal to the saturation value. The height at which this happens is called the Lifting Condensation Level (LCL). Any higher than this point and the parcel becomes less buoyant than the environment so there is no more driving force. Because of this the parcel starts to decelerate. However, the parcel gained kinetic energy while rising, and if the parcel has enough kinetic energy it continues to rise above the LCL. During this time more water condensates, and the energy that is released acts as a buoyancy generator for the parcel. The parcel follows the moist adiabatic lapse rate instead of the dry adiabatic lapse rate because of the condensation process.
If enough kinetic energy is present the parcel rises high enough to reach the Level of Free Convection (LFC). At this height the parcel is positively buoyant again, so the parcel rises freely. If the parcel rises high enough it reaches the inversion layer at the Level of Neutral Buoyancy (LNB) and above the LNB the parcel is less buoyant than the environment. If enough kinetic energy is present the parcel can penetrate for some distance into the inversion layer, but for BOMEX the inversion layer is strong enough to stop the thermal from rising above the inversion layer.

3.1.2 The critical mixing fraction

Cloudy air and environmental air are continuously mixing. As a measure of this mixing, the mixing fraction χ is introduced. χ is defined as the fraction of environmental air that is present in a mixture of updraft air and environmental air.

$$\chi = \frac{m_{env}}{m_{env} + m_{up}} \tag{3.6}$$

Where m_{env} is the mass of the environmental air in the mixture and m_{up} the mass of the updraft air in the mixture. So χ equals zero for a mixture that contains updraft air only, and χ equals one for a mixture that contains environmental air only.

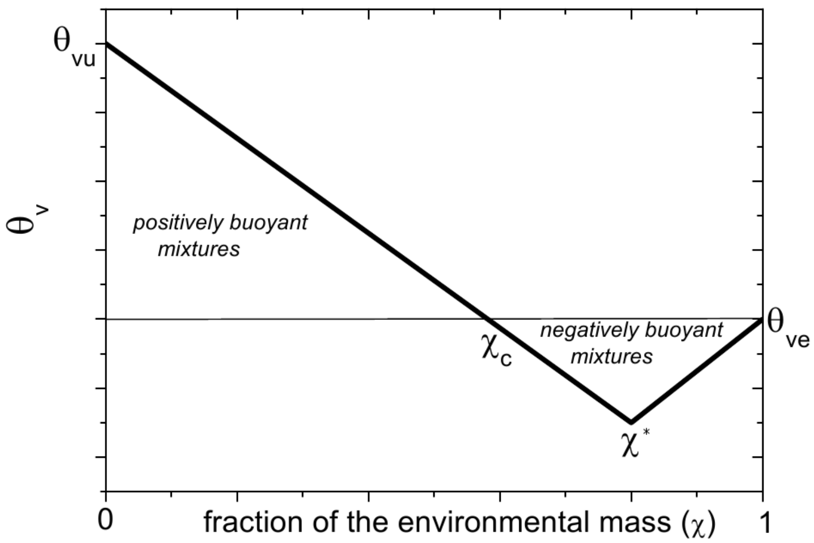

Figure 3.2: χ **vs** θ_v**, courtesy of de Rooy and Siebesma (2007)**

Figure 3.2 illustrates the relation between the mixing fraction χ and the virtual potential temperature θ_v. When mixing more and more environmental air in the mixture, the air in the mixture gets dryer and the liquid water in the mixture starts to evaporate. Since condensation releases heat, evaporation needs heat and thus leads to cooling. Because of this cooling the line between $\chi = 0$ and $\chi = 1$ is not a straight line, but it exhibits a minimum at a point χ^*. At this minimum all the liquid water is evaporated. The mixture of air that is neutrally buoyant is called the critical mixing fraction $\chi_{critical}$, from now on abbreviated as χ_c. The mixtures between $\chi = \chi_c$ and $\chi = 1$ are negatively buoyant because of the evaporative cooling.
The goal of this section is to give an expression for χ_c purely in terms of environmental and updraft variables, since this means that χ_c can be used as a measure of the mean state of the system. A parcel of mixed air containing a fraction χ of environmental air and a fraction $1 - \chi$ of updraft air has a virtual potential temperature given by

$$\theta_v(\chi) = \theta(\chi) \cdot (1 + \lambda \cdot q_v(\chi) - q_l(\chi)) \tag{3.7}$$

Where θ_v is the virtual potential temperature, θ is the potential temperature, q_v is the water vapor specific humidity and q_l is the liquid water specific humidity. θ is given by (2.3) and λ is given by (2.6)

The variables θ_l and q_t are moist conserved variables, which means that they mix linearly. This means that these variables can be written as a combination of environmental and updraft air:

$$\theta_l(\chi) = \theta_{lu} - \chi \cdot (\theta_{lu} - \theta_{le}) = \theta_{lu} - \chi \cdot d\theta_l \tag{3.8}$$
$$q_t(\chi) = q_{tu} - \chi \cdot (q_{tu} - q_{te}) = q_{tu} - \chi \cdot dq_t \tag{3.9}$$

where the subscript e stands for environment and u for updraft. Please note that in this report the updraft variables are approximated by conditionally sampling that variable by using (2.50).

By using (2.1) and (2.3) an expressions for q_v and θ in terms of moisture conserved variables can be obtained. Using these expressions in (3.7) and leaving out the higher order moisture terms then gives:

$$\theta_v(\chi) = \theta_l(\chi) \cdot (1 + \lambda \cdot q_t(\chi) - (1+\lambda) \cdot q_l(\chi)) + \frac{L_v}{c_p \pi} \cdot q_l(\chi) \tag{3.10}$$

The liquid water specific humidity in (3.10) is not moist conserved, so q_l can not be written as a linear combination of environmental and updraft air. Another way to write q_l as a combination of these terms is to start by writing q_l as

$$q_l(\chi) = q_t(\chi) - q_s(p, T(\chi)) \tag{3.11}$$

Which is valid as long as the mixture contains liquid water. In (3.11) q_{sat} stands for the saturation-specific humidity that depends on pressure p and the temperature T of the mixture. Using a Taylor expansion around $T(\chi = 0) = T_u$ gives the following expression

$$q_s(T(\chi)) \;\; = q_s(T_u) + (T(\chi) - T_u) \cdot \frac{dq_s}{dT}|_{T_u} \tag{3.12}$$

Inserting this equation in (3.11) and using (2.1) this then gives

$$q_l(\chi) = q_{lu} - \frac{\chi}{1+\gamma} \cdot (dq_t - \gamma dt_l) \tag{3.13}$$

$$\gamma = \frac{L}{c_p} \frac{dq_s}{dT}|_{T_u} \tag{3.14}$$

By using (3.8), (3.9) and (3.10) an expression for θ_v purely as a combination of updraft and environmental variables can be deduced:

$$\theta_v(\chi) = \theta_{vu} - \chi \cdot (\beta \cdot d\theta_l + dq_t \cdot (\beta - \alpha) \frac{L_v}{c_p \pi}) \tag{3.15}$$

with

$$\beta = \frac{1}{1+\gamma} \cdot (1 + (1+\lambda)\gamma\alpha) \tag{3.16}$$

$$\alpha = \frac{c_p}{L_v} \pi \theta_{lu} \tag{3.17}$$

$d\theta_l$ and dq_t represent the updraft excesses of the respective variables. $\chi_{critical}$ is defined as the mixing point at which the buoyancy of a packet of air is neutral compared to the environment. Making use of this definition an expression for χ_c can be found by rewriting (3.15)

$$\chi_c = \frac{d\theta_v}{\beta d\theta_l + dq_t(\beta - \alpha)\frac{L_v}{c_p \pi}} \tag{3.18}$$

Where $d\theta_v$ is the updraft buoyancy excess.

It is known from literature that there exists a relationship between χ_c and the convection response (de Rooy and Siebesma, 2007). The convection response is an indication of how easily clouds form in a response to convective circumstances. In this report the convection response is quantified through a nondimensionalized mass flux m^*. The definition of m^* is given by

$$m^* = \frac{m(\frac{z_t - z_b}{2})}{m(z_b)} \tag{3.19}$$

which is just the mass flux halfway the cloud divided by the mass flux at the cloudbase. The subscript t stands for cloud-top and b stands for cloud-base. This means that m^* is smaller than one, since in this report the cloudbase for shallow cumulus is defined as the height at which the mass flux is at a maximum. As to why m^* is a measure for the convection response can easily be seen by imagining what happens when more deep clouds form (so the convection response is increased). This means that the gradient of the ensemble mass flux in the cloudlayer is less steep than before and so the m^* increases. The relation between χ_c and m^* is illustrated in figure 3.3.

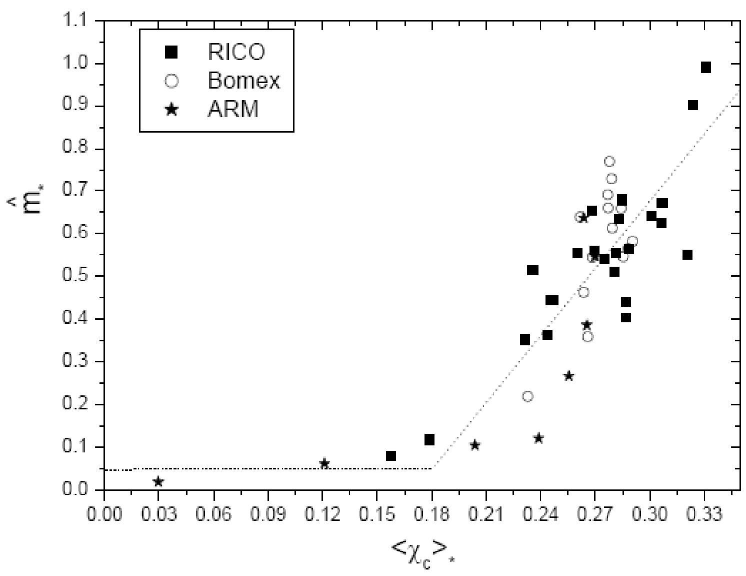

Figure 3.3: Relationship between χ_c and $m*$ from LES experiments for different cases, courtesy of de Rooy and Siebesma (2007)

As can be noted from this figure, the χ_c values for the BOMEX case only covers a small range. The relationship that is sketched by the dotted line is therefore not apparent for BOMEX only, so a way is needed to get more variability in χ_c. This is done by perturbing the standard BOMEX case, which is the subject of section 3.3.

3.1.3 Normalized moist buoyancy deficit

Another way to describe the state of the system statistically through a single variable is with the normalized moist buoyancy deficit Q_c. This normalized moist buoyancy deficit is given by (Neggers et al., 2009)

$$Q_c = \frac{q_t(\chi_c) - \overline{q_t}}{\sigma_{q_t}} \tag{3.20}$$

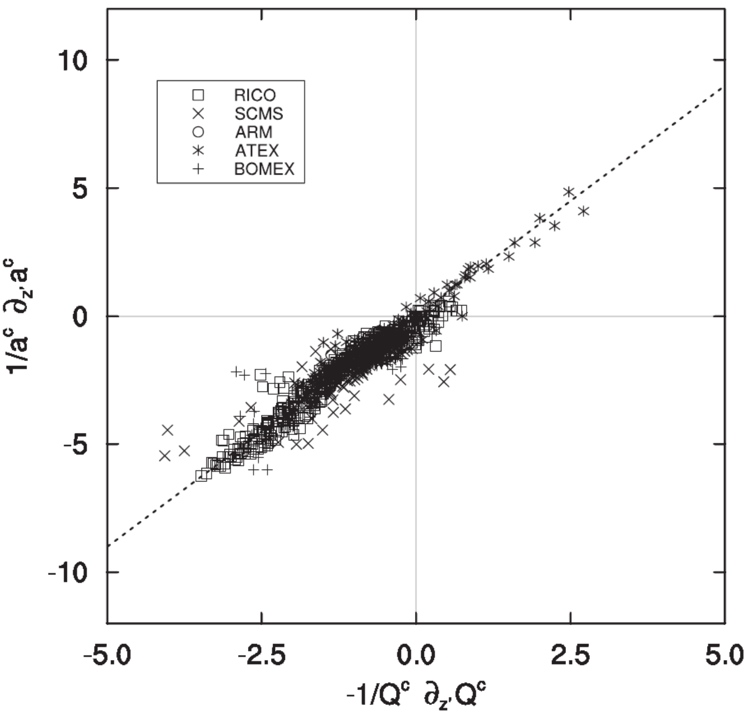

Figure 3.4: The relation between the normalized moist buoyancy deficit and the cloud core fraction. Courtesy of Neggers et al. (2009).

Where $q_t(\chi_c)$ is the total specific humidity at a mixing fraction χ_c and σ_{q_t} is the standard deviation of the total specific humidity. To make it easier to calculate Q_c from variables that are directly available from the simulation output files, this equation is rewritten. The $q_t(\chi_c)$ term can be written as

$$q_t(\chi_c) = q_{t,c} \cdot \chi_c + (1 - \chi_c)\overline{q_t} \tag{3.21}$$

Inserting this in equation (3.20) gives

$$Q_c = \frac{\chi_c \cdot (q_{t,c} - \overline{q_t})}{\sigma_{q_t}} \tag{3.22}$$

Which can be calculated directly from the simulation output files. As suggested by Neggers et al. (2009), a correlation exists between the cloud core cover a_c and Q_c for shallow cumulus convection. This relation is given to be

$$\frac{1}{a_c}\frac{\partial a_c}{\partial z'} = C_a \frac{1}{Q_c}\frac{\partial Q_c}{\partial z'} \tag{3.23}$$

Where z' is the height above the cloudbase normalized by the cloud layer depth. Neggers et al. (2009) found that a strong correlation exists and C_a is determined to be -1.8 from the data. This relation is currently tested to be used in weather forecast models, so it is interesting to see how this relation behaves when the BOMEX case is perturbed, on which more information is given in section 3.3.

3.2 Subdomain Analysis for mean state variables

When dividing the domain in subdomains, it is not always trivial what is meant by a spatial average. A spatial average can mean that a value has been averaged over the entire horizontal domain, or over a single subdomain. When calculating the mean state variables the difference between the average value of, for example, θ_v on a horizontal domain and the local value of θ_v in a single gridpoint is needed. On a full domain this difference is clear, but when dealing with subdomains one can either use the average over the full domain, or the average on a subdomain. Especially when the subdomain size decreases the difference between these two approaches is expected to increase. In the limit of very small subdomains this essentially means that the average value of a variable on the subdomain converges to the value of that variable in a single gridbox.
In this report the subdomain averages are used when an average is used in a formula. The reason is that the subdomains directly represent the change in resolution. Since the full domain average does not change, it is not correct to use the full domain average.

3.3 Perturbed BOMEX

Because BOMEX is a steady state shallow cumulus case with only a small cloud cover it might be interesting to consider some other cases as well. In order to keep good track of the differences between cases, the standard BOMEX case is perturbed in different ways. This way an attempt is made to get a larger variation in the parameters involved, and hopefully this provides more information about the way the parametrization behaves. In the following sections three different 'types' of perturbing are considered. The first is to apply a constant perturbation to the initial profiles. The second way is to perturb the gradients of the initial profiles, and the last way that is considered is to keep a constant relative humidity at vertical levels above the cloudbase.

3.3.1 Perturbation of initial profiles

Perturbing the BOMEX case can happen in many ways. The first way discussed here is a constant perturbation of certain initial profiles. The initial input profiles of θ and q are perturbed in such a way that the profile of θ_v stays the same. This also means that CAPE and CIN stay the same, since these are directly related to the θ_v profile. This ensures that the system is in more or less the same state as before (the same potential energy is present for cloud formation). According to equation (2.5) the θ_v profile is directly dependent on θ and q. To keep matters simple, it is assumed for now that there is no liquid water present, so $q_l = 0$. This means that all the water present is in the gas state, so $q = q_v$. This way a very simple relationship follows:

$$\theta_v = \theta \cdot (1 + \lambda q) \tag{3.24}$$

with $\lambda \approx 0.61$, see equation (2.6). Since the goal is to make a perturbation to the input profiles, the relationship between the differences of these variables is more interesting. Since this is a linear equation the perturbations can be directly put in:

$$\theta_v + \delta\theta_v = (\theta + \delta\theta) \cdot (1 + \lambda(q + \delta q)) \tag{3.25}$$

In this equation the perturbation in θ_v is of course zero, because the goal is to keep the θ_v profile the same. Rewriting gives the following relation between the perturbation of q and the perturbation of θ

$$\delta q = -\delta\theta \frac{1 + \lambda q}{\lambda\theta} \tag{3.26}$$

The value of θ and q at the surface (for BOMEX: 297.8 K and 17 g/kg) is then used in equation (3.26) because the θ and q profiles in the mixed layer are almost constant. With that the relationship between $\delta\theta$ and δq is complete

$$\delta q \approx \frac{-\delta\theta}{180} \tag{3.27}$$

Since de Roode et al. (2005) also performed similar experiments, the initial profiles used there are also used here as a starting point. Details about the cases for the constant perturbation of input profiles can be found in section 5.1. It should be noted that this approach has some limitations. It is known that BOMEX simulation that are perturbed through initial profiles tend to go back to the original BOMEX profiles over time. This means that it is useless to run a perturbed simulation for a long period of time, since this results in the original BOMEX simulation. To avoid this problem, only short simulation are performed, and only the first hours after the startup phase are considered in the analysis.

3.3.2 Perturbations of the gradients

The second way that is used to perturb the initial profiles is to perturb the gradients of the profiles instead of a constant perturbation. The aim still is to keep the θ_v profile (and thus gradient) the same as before to keep the CIN/CAPE the same. The same reasoning as in 3.3.1 applies here, but now to the gradients. Using equation (3.24) again but now for gradients:

$$\Gamma_{\theta_v} = \Gamma_\theta \cdot (1 + \lambda\Gamma_q) \tag{3.28}$$

this can then be written in the same way if perturbations are put in

$$\Gamma_{\theta_v} + \delta\Gamma_{\theta_v} = (\Gamma_\theta + \delta\Gamma_\theta) \cdot (1 + \lambda(\Gamma_q + \delta\Gamma_q)) \tag{3.29}$$

Again the idea is to keep the θ_v gradient the same as before, so $\delta\Gamma_{\theta_v}$ is zero. Rewriting thus gives a similar expression to (3.26)

$$\delta\Gamma_q = -\delta\Gamma_\theta \frac{1 + \lambda\Gamma_q}{\lambda\Gamma_\theta} \tag{3.30}$$

This expression is then used for the known Γ_θ and Γ_q in the cloud layer. For BOMEX the cloud-layer gradients are Γ_θ = 3.9 K/km and Γ_q = -5.8 g/kg/km. With this information several cases can be set up, again perturbing the input profiles. Again the same as in the previous section applies: the profiles tend to go back to the original BOMEX profiles so only short simulations are used. More information about the input profiles and the results for these cases can be found in section 5.2.

3.3.3 Relative humidity

Up till now, all the perturbations had some restrictions regarding the θ_v profile. In this section a whole different approach is used, with the relative humidity as the restriction. As a starting point for setting up these cases the work from de Roode (2007) is used. In this paper exact equations for the mixing ratio as a function of the lapse rates of q and θ are derived, and figure 3.5 is presented. It should be noted that the relations

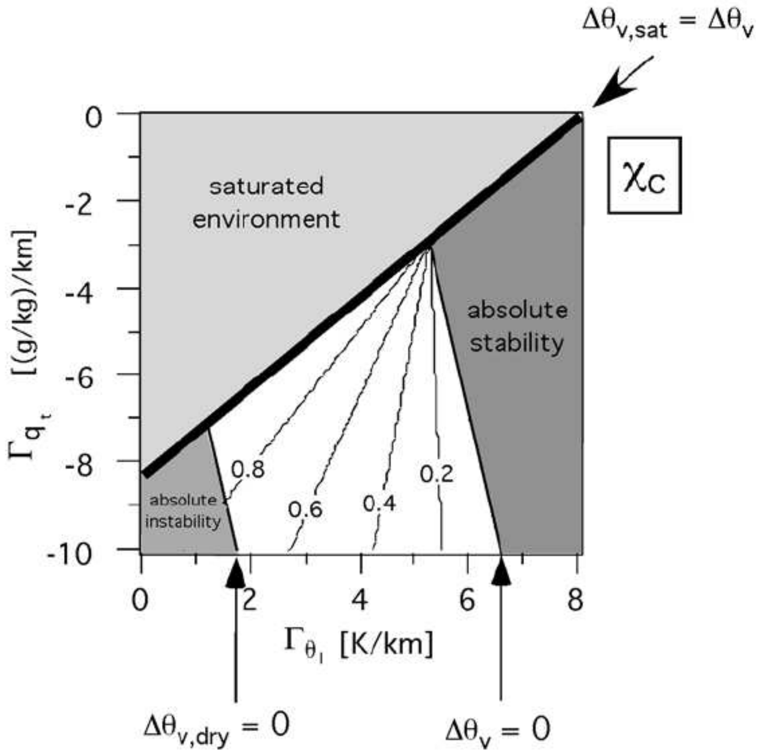

Figure 3.5: Contourplot of χ_c as a function of the mean vertical lapse rates Γ_q and Γ_θ, taken from de Roode (2007).

in this figure hold for a parcel that is rising adiabatically, so the values in the figure do not exactly 'match' reality. The part of the figure that is not grey is the area that is interesting, since this area represents shallow cumulus convection. The typical lapse rates for BOMEX (Γ_θ = 3.9 K/km and Γ_q = -5.8 g/kg/km) indicate that BOMEX lies somewhere in the middle of the white area. The idea is to explore other parts of this white area to get a larger subset of χ_c values. A way to explore this area is inspired by Derbyshire et al. (2004) who investigated the sensitivity of Cloud Resolving Models (CRMs) and Single Column Models (SCMs) to humidity. This is done by setting a constant value for the Relative Humidity (RH) in the cloud layer and above. The results in this paper show that the Relative Humidity has a very large influence on the dynamics of the simulation.

With this in mind, figure 3.5 is presented in another way here. Instead of the lapse rate of the specific humidity on the y-axis, the mixing fraction as a function of relative humidity is calculated, again assuming an adiabatic parcel. The relative humidity is set to a certain value by using equation (2.19). The total specific humidity is simply set to a value that is a certain percentage of the saturation specific humidity. Repeating this for the same range of θ lapse rates as in figure 3.5, figure 3.6 is obtained.

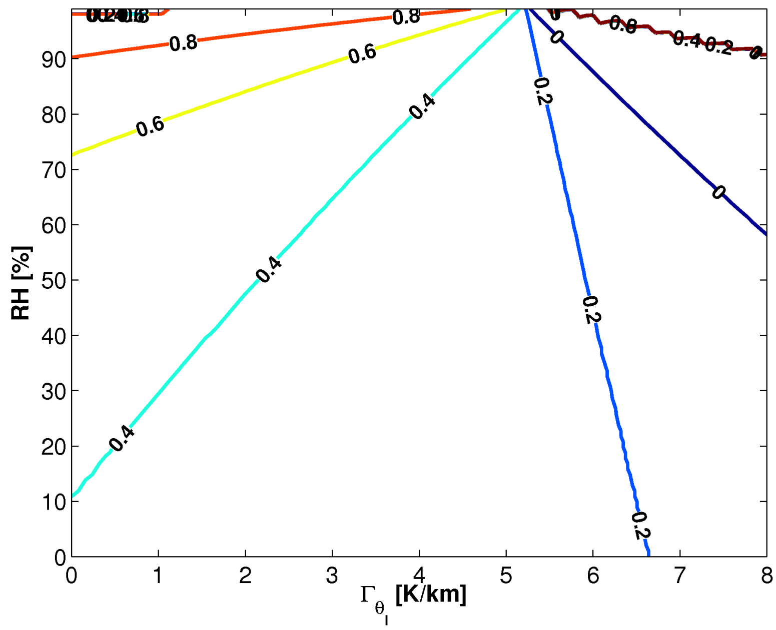

Figure 3.6: A contourplot of the critical mixing ratio as a function of the lapse rate of the virtual temperature and the relative humidity at a height of 900m, assuming an adiabatic parcel.

This figure can basically be seen as a deformed enlargement of the white area in figure 3.5, since the saturated regime lies in the area where the relative humidity is larger than 100%, so this is not displayed anymore in figure 3.6. The regime of absolute stability is still visible in the upper right corner, while the absolute unstable regime is located in the far left corner. This way, the only really well visible regime is the cumulus regime, which is the regime of interest. The BOMEX case is located in the upper-middle part of the figure (RH $\sim$ 75% and $\Gamma_{\theta_l} \sim 3.9$K/km). The figure shows that a good way to get more variability in the χ_c values is to change the relative humidity. Changing the temperature would of course also give an effect but would also mean that the CAPE and CIN are not kept the same anymore. Furthermore the relative humidity is found to vary greatly in nature, as for example is found in measurements in de Arellano (2007). To investigate the effects of the relative humidity 10 runs are set up. The values of the RH are varied between 20% and 95% in the cloud layer and above in the different runs. Figure 3.7 shows the relative humidities and the corresponding q_t input profiles for these runs. The input profile of θ_l is kept the same as in the original BOMEX, and because an inversion is present in this input profile this translates to nonlinear behaviour of the q_t profile, since the relative humidity is a function of both the temperature and humidity as seen in setion 2.1.3.

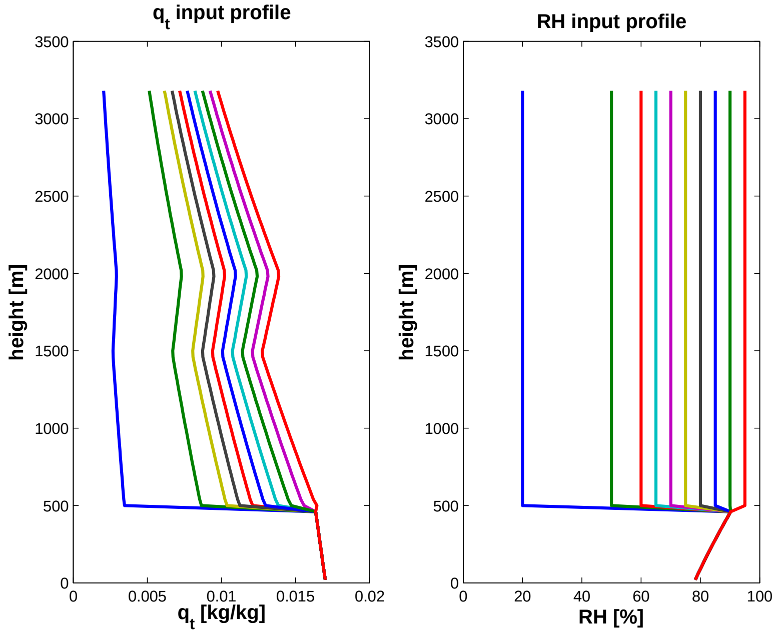

Figure 3.7: The input profiles used for the RH sensitivity runs. Below the cloud layer the original q_t profiles is used, above the RH is set to a constant value, varying between 20 and 95 for the different runs. More cases with higher relative humidities are used, since figure 3.6 shows that χ_c changes the most for higher relative humidities. The θ_l input profile was not changed, which explains the nonlinear behaviour of the q_t profile since the inversion is still present in the θ_l profile.

The results from these simulations can then be used to investigate the correlation between χ_c and m^*, and to see how the entrainment and detrainment vary as a function of the relative humidity, and thus also as a function of χ_c. Bretherton et al. (2004) finds that a correlation is expected between the entrainment/detrainment and χ_c. This correlation is hypothesized to be

$$\begin{aligned} \epsilon &= \epsilon_0 \chi_c^2 \\ \delta &= \delta_0 (1 - \chi_c^2) \end{aligned} \tag{3.31}$$

where ϵ_0 and δ_0 are dependent on the height. Equation (3.31) is investigated with the results from the simulations. Furthermore the relation between Q_c and a_c from equation (3.23) is also be tested for the perturbed BOMEX cases.

Chapter 4

Results subdomain analysis

In this chapter the results for the subdomain analysis described in chapter 2.6 are presented. In the first section the LES is briefly tested against the results from the stratocumulus measurements (Wood et al., 2002). After that the BOMEX case is analyzed to see if any subdomain dependence exists.

4.1 Variances of thermodynamic variables

4.1.1 Validation of the stratocumulus case

As shown in section 2.6.2 measurements show that the variance of s has a correlation with the size of a subdomain. This relation is first tested with DALES for the stratocumulus FIRE case that is used in the paper of Wood et al. (2002). For this purpose a 48-hour run on a $256 \times 256 \times 64$ domain, $25.6 \times 25.6 \times 0.64$ km is used. The plot that reproduces the relation between the standard deviation of s and the domain size is shown in figure 4.1

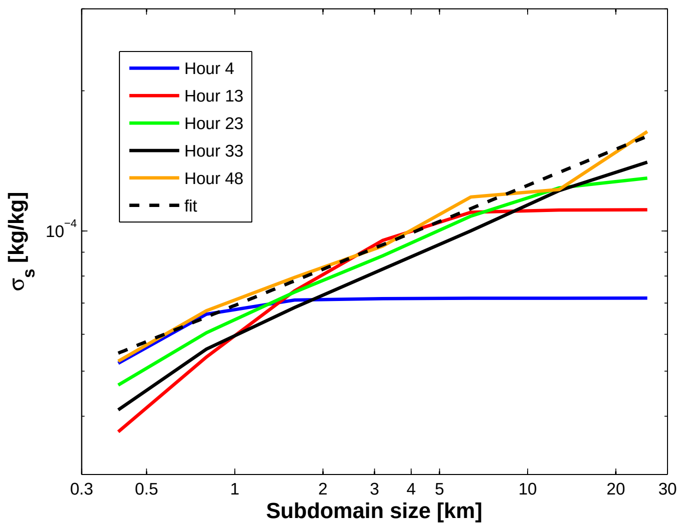

Figure 4.1: The standard deviation of s plotted against the subdomain size for the stratocumulus FIRE case. The different lines show the variance for different hours of the simulation. In the figure the fitted powerlaw is shown as the dotted black line.

As can be noted from figure 4.1, the variance grows over time. especially on the large scales. After about 24 hours the growth starts to diminish, and the graph is less steep than expected from the measurements from Wood et al. (2002). The constant β_S (see equation (2.63)) is fitted through matlab using a unconstrained nonlinear minimisation of the SSR (sum of squared residuals) with respect to the various parameters and is determined to be 0.26 with a correlation coefficient R of 0.99 for hour 48. The correlation coefficient is a measure of how well the fitted points fit the data, if R equals 1 then the fitted function fits the data perfectly, if R equals 0 then the fitted function does not fit the data at all. Mathematically R is defined as

$$R = \left(\frac{\sum (y_{fit} - \overline{y})^2}{\sum (y_{fit} - y)^2 + \sum (y_{fit} - \overline{y})^2} \right)^{1/2} \tag{4.1}$$

From figure 4.1 it follows that the LES gives a good estimation of the standard deviation of s for stratocumulus, so the same analysis is repeated for BOMEX. Next the standard deviation of q_t is plotted in figure 4.2 to see how the variance of a single variable behaves.

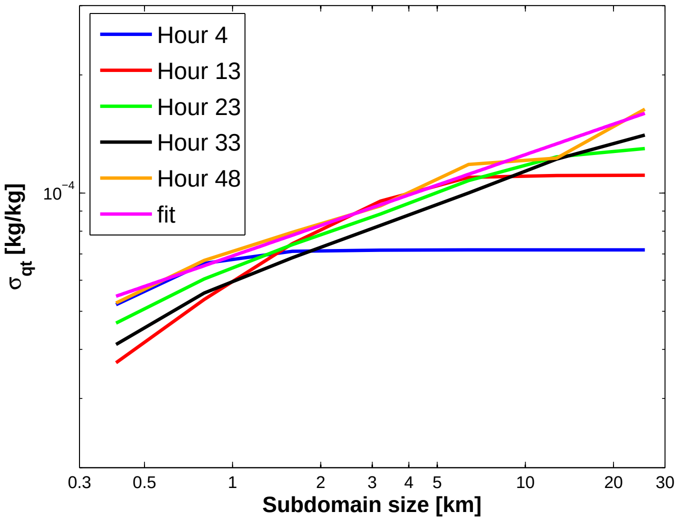

Figure 4.2: The standard deviation of q_t as a function of the subdomain size. The different lines represent different times in the simulation. The power law fitted to hour 48 is shown as the dotted black line.

As can be seen from the figure the standard deviation of q_t behaves just like s, the same growth over time is observed as with s as well. The constant β_S is determined to be 0.26 through a fit for four 48, with a correlation coefficient R of 0.99. Since this is the same constant as was found for the standard deviation of s the total specific humidity is used for the analysis of the BOMEX case (as both s and q_t show the same domain size dependence).

4.1.2 Variances BOMEX

The first run that is analysed is a run on a very large domain, 1024×1024×80, 25×25×3.2 km. Since the domain contains a large amount of gridpoints, the simulation is only run for 5 hours because of computational cost. This domain is then divided into subdomains

as described in section 2.6.1.
The variances of several variables are presented in figure 4.3. As the figure shows, the variances of these thermodynamic variables behave different from the variance of the FIRE case. In the FIRE case, the variance grows as the domain size grows, but for the BOMEX case the variances stay more or less constant on the larger subdomains, only as the subdomain size reaches 1km the variance start to show some decrease. This decrease is of course expected, since in the limit of the subdomain size to the size of a single gridpoint the variance is zero.

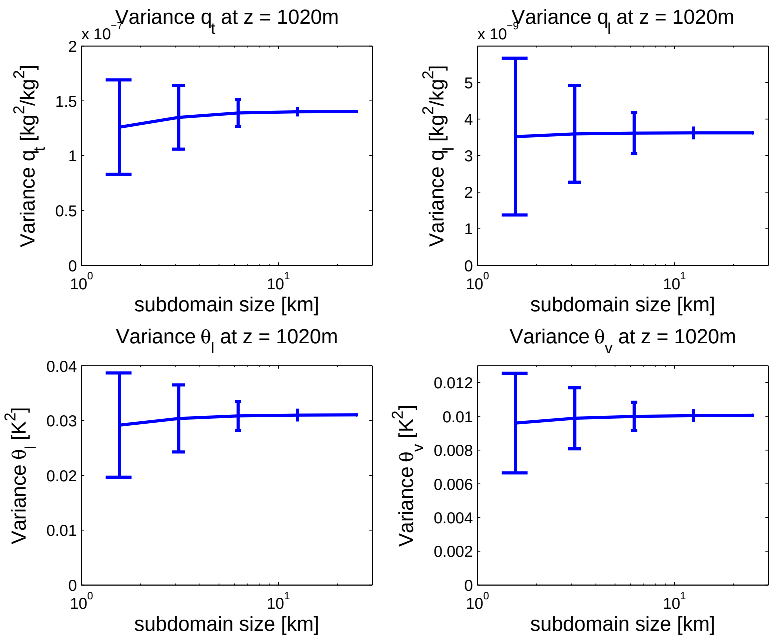

Figure 4.3: The variance of the different thermodynamic variables as a function of the size of the subdomains. The vertical bars represent the error in the mean value given by two times the standard deviation.

The FIRE case only shows the power-law behaviour after running the simulation a large amount of time, so a test is needed to see if the BOMEX case also behaves in this way. Therefore a 24-hour BOMEX run is performed, but to keep the computational cost limited, the number of gridpoints is reduced to $256 \times 256 \times 80$, $25 \times 25 \times 3.2$ km. The result for the variance of q_t is shown in figure 4.4.

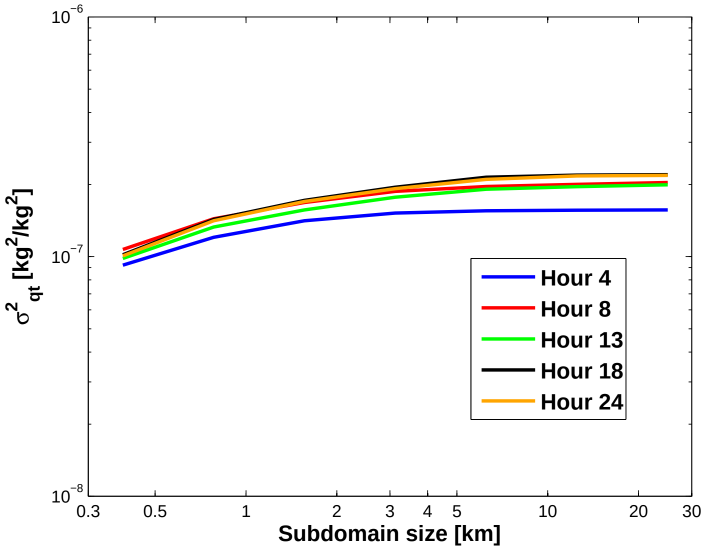

Figure 4.4: The variance of q_t for a 24-hour BOMEX run as a function of subdomain size. The different lines show the variance for different hours of the simulation.

It is clear from this figure that the scale dependence that is observed in the stratocumulus case is not visible here. Even for longer periods the the power-law does not apply to the BOMEX case. A growth of variance over time would probably mean that BOMEX also starts to show a scale-dependence, but for now it is unclear why the BOMEX case behaves in this way.

4.2 Parametrized variables

Since no clear correlation is visible between the variance of the thermodynamic variables and the subdomain size, the next step is to directly observe the parametrization variables ϵ and δ.

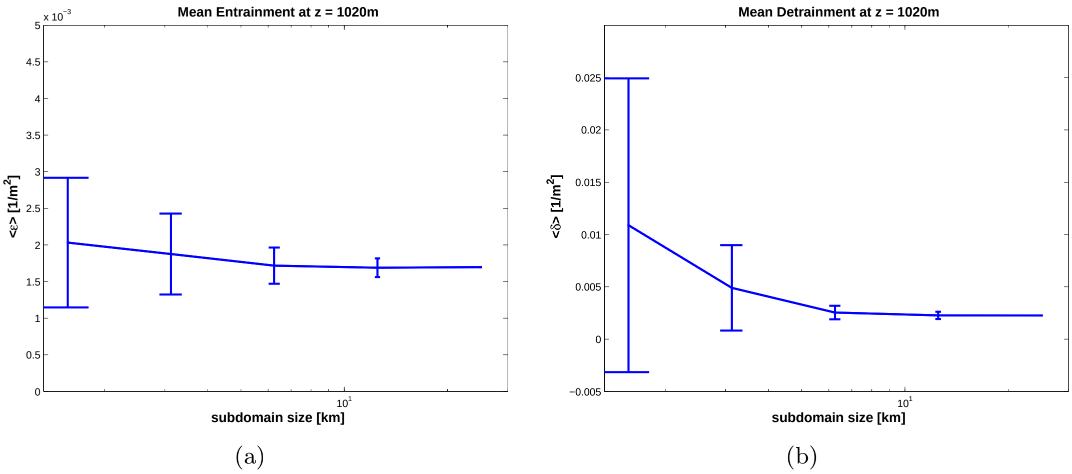

Figure 4.5: The diagnosed entrainment (a) and detrainment (b) rates vs the subdomain size.

This is done for the simulation with domainsize $1024 \times 1024 \times 80$, $25 \times 25 \times 3.2$ km. The 3D output fields are used to create the figures, so a lot of spatial information is available, but the fields are instantaneous so the time averaging is rough (section 2.3). In figure 4.5 the average entrainment and detrainment against the subdomain size is shown. The change of the diagnosed entrainment and detrainment rates as a function of subdomain size is not clearly visible, some change might be happening near the smaller subdomains (especially the detrainment) but the spread in the variables is so large that no conclusion can be made. Please note that mathematically there is not reason why the detrainment cannot reach values below zero, as mentioned before in section 2.5.2. This probably happens here because on the smaller subdomains some 'artifacts' occur in the way the entrainment is diagnosed. The derivative $\frac{dq_{t,c}}{dz}$ might vary a lot on the smaller subdomains, so that the value for the entrainment can get very low. The detrainment is diagnosed simply by subtracting $(\frac{dm_c}{dz})/m_c$ from the entrainment. So if this latter term is larger than the entrainment then the detrainment is diagnosed to be negative on this particular subdomain. Apparently this happens often enough to get several negative values for the detrainment. There is however no physical reason for the negative values of the detrainment.

4.3 Mean state variables

Since the diagnosed entrainment and detrainment rates do not show a clear correlation for the BOMEX case, the mean state variables are examined. The way these variables are calculated is described in chapter 3. First the CAPE and CIN as a function of subdomains size are shown in figure 4.6.

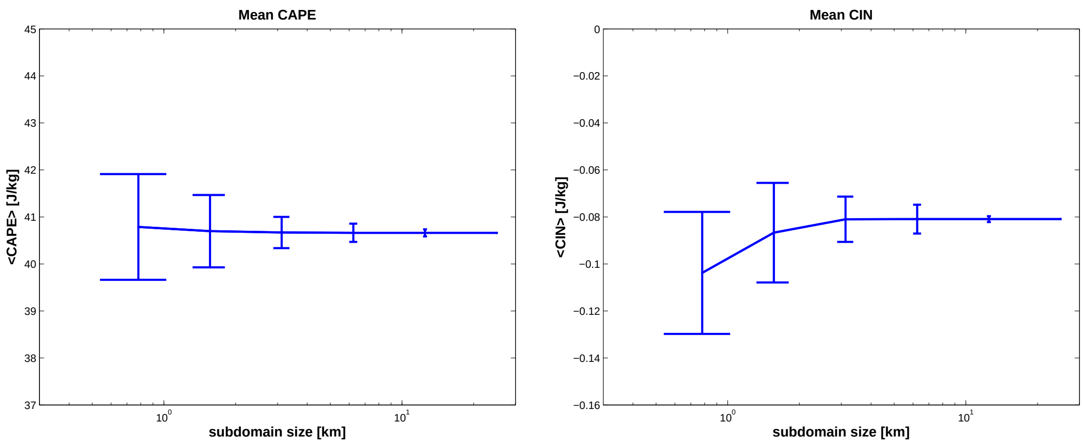

(a) (b)

Figure 4.6: The mean state variables CAPE (a) and CIN (b) vs the subdomain size.

Again these results are from the simulation on a very large domain. These figures essentially show the same behaviour as with the diagnosed entrainment and detrainment rates, some change is visible. But because of the spread in the variables no conclusion can be made about any correlation between CAPE or CIN and the subdomain size. A careful first conclusion could be that CAPE is not dependent on the subdomain size, but that CIN might have some dependence, even though the spread is so large. Statistically speaking the CIN does not change with the subdomain size because the value of the CIN on the full domain is within the errorbar of the CIN on the smallest subdomain. Another way to look at CAPE or CIN is to see if a relationship exists between these mean state variables and the convection response. For every subdomain size, a scatterplot of CAPE and CIN against m^* is made, and these plots are shown in 4.7 and 4.8.

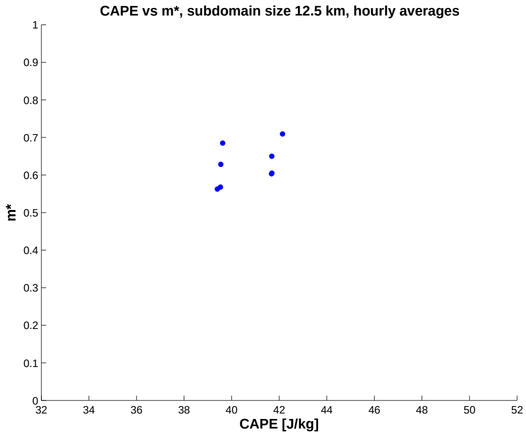

(a)

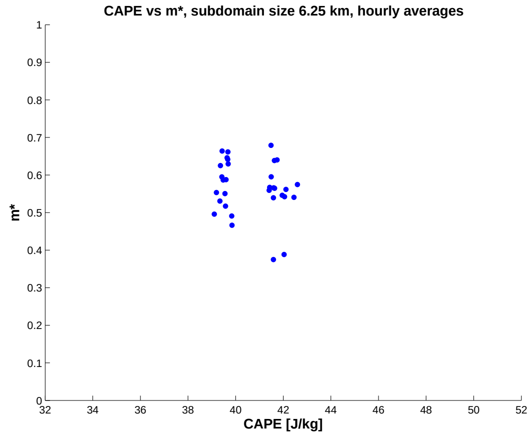

(b)

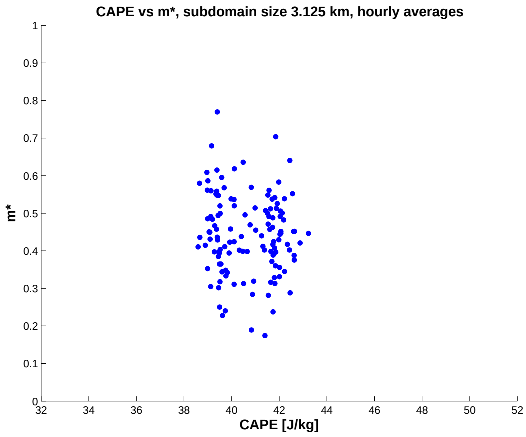

(c)

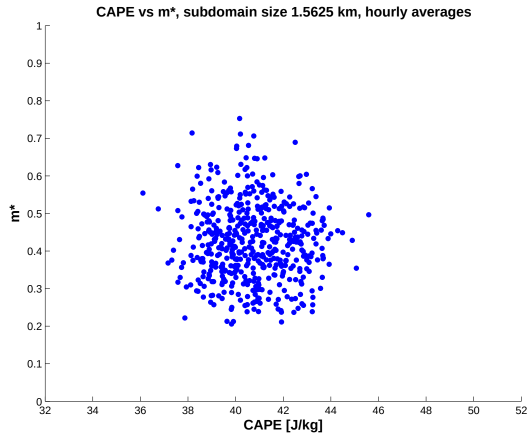

(d)

Figure 4.7: CAPE vs m* for different subdomain sizes (the length in km. is the length of one horizontal side of the subdomain). The values are averages over one hour of 6 instantaneous fields.)

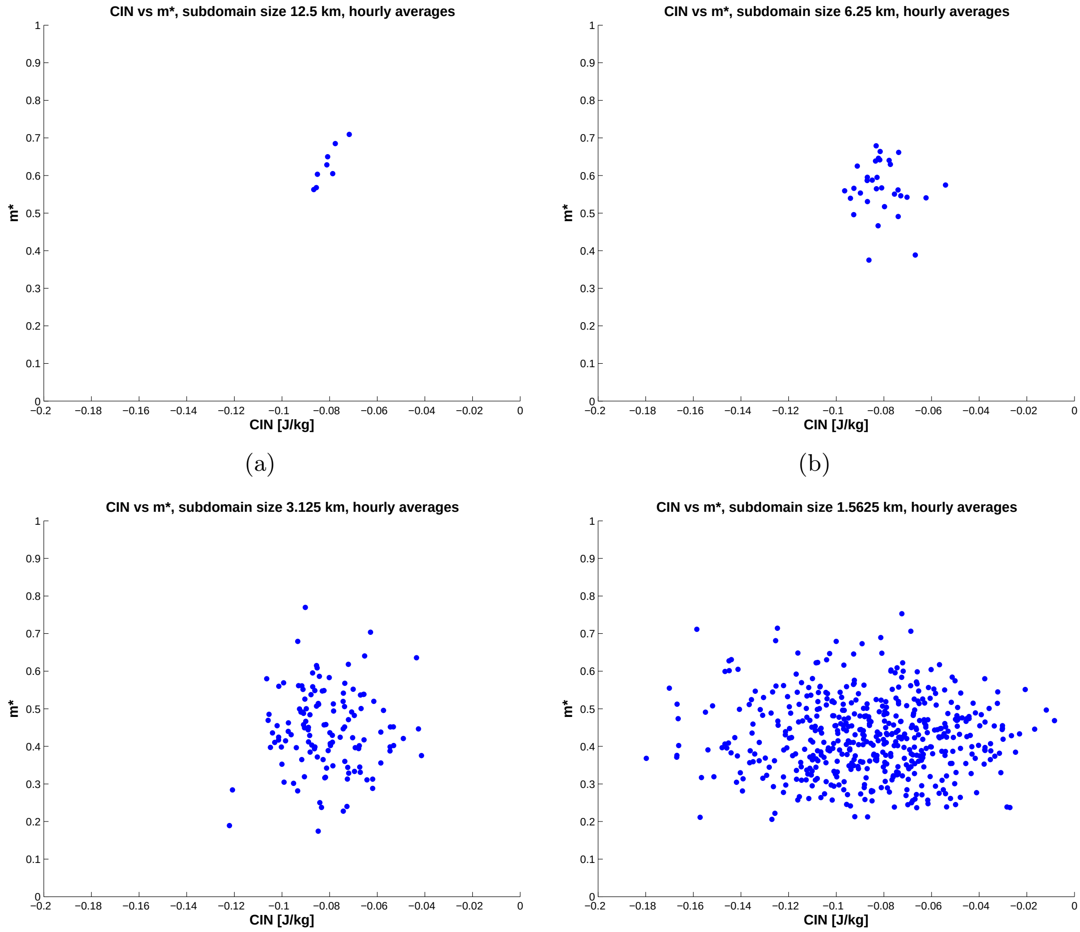

(a) (b) (c) (d)

Figure 4.8: CIN vs m* for different subdomain sizes (the length in km. is the length of one horizontal side of the subdomain). The values are averages over one hour of 6 instantaneous fields.)

Even though the cloud of points grows with every next plot, the position of the mean does not seem to differ much. This could mean that the CAPE and CIN are not correlated with the subdomain size. Figure 4.8 also shows the even though the mean of CIN shifts a bit in the lower right plot, the spread also increases a lot. This indicates that the the change of CIN as a function of subdomain size as suggested in figure 4.6 really is not statistically existing. The plots from the CAPE and CIN do not show any clear correlation with m^* or the subdomain size, so a different mean state variable is examined. As discussed in section 3.1.2, it is known from theory (de Rooy and Siebesma, 2007) that a correlation exists between the critical mixing fraction χ_c and m^*. To see if this correlation holds for different subdomains, the plots in figure 4.9 are made. The values shown there are averages over one hour of 6 instantaneous fields.

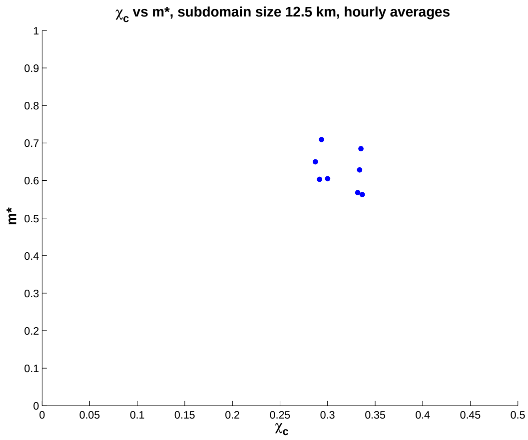

(a)

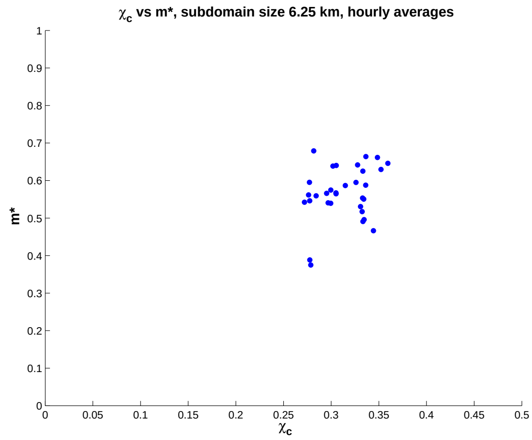

(b)

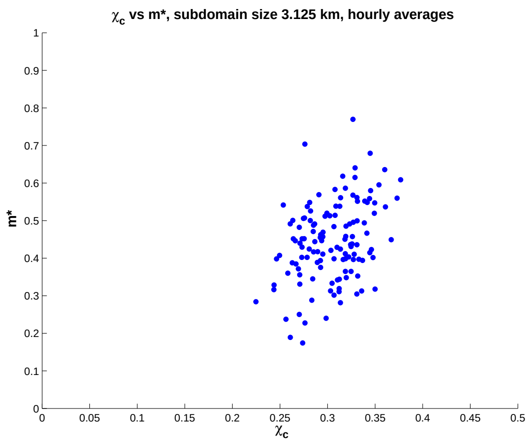

(c)

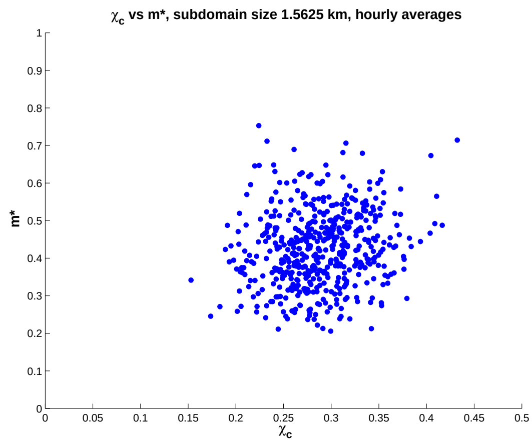

(d)

Figure 4.9: χ_c vs m* for different subdomain sizes (the length in km. is the length of one horizontal side of the subdomain).)

As can be seen from these figures, the mean of the values for χ_c does coincide with the value found by de Rooy and Siebesma (2007), but the correlation between χ_c and m^* is not visible. The mean values of χ_c do not seem to vary much between the different subdomain sizes, which is expected because the BOMEX case that is used here is in a steady-state. So all that seems to happen is an increase in spread, just like with the CAPE and CIN. This could indicate that χ_c might not depend on the subdomain size, just like CAPE and CIN.

Because the results for the subdomain analysis do not show the correlation from de Rooy and Siebesma (2007) the same figure is made again to see if the correlation exists when time-averaging over more values. So this time the time-averaged output fields are used instead of the 3D output fields, see section 2.3. The result from a LES run with domain-size 128*128*80, 6.4*6.4*3.2km is shown in figure 4.10.

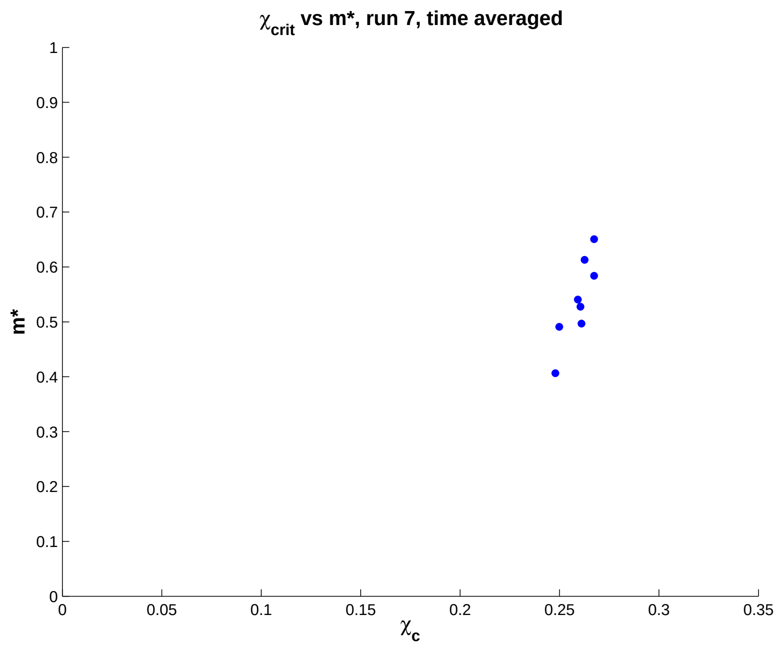

Figure 4.10: The relationship between χ_c and m^* from the LES, the points are hourly averages.

So this shows that a relationship between χ_c and m^* is indeed present, but apparently it is only clearly visible when averaging with more timesteps so that the statistics are better. It is hard to see if the correlation from de Rooy and Siebesma (2007) completely holds because the values for χ_c for the standard BOMEX case do not show much variation, especially the part for the lower χ_c values is hard to check. The same plots can be made for the CAPE and CIN, this time also with better time statistics from the smaller run. The results are shown in figure 4.11.

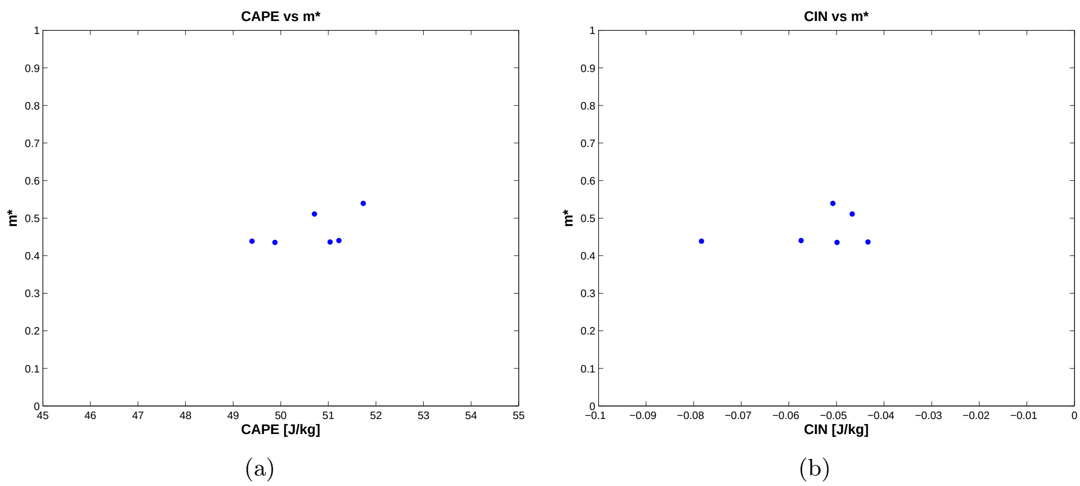

Figure 4.11: The mean state variables CAPE (a) and CIN (b) vs the subdomain size.

As can be seen from this figure still no relation is visible between the CAPE or CIN and $m*$. It is therefore probable that no relationship exists, or that it is simply not visible for the current state of the system. Therefore the standard BOMEX case is perturbed in the next section to try to get more variation in the values of χ_c, CAPE and CIN. At the same time the (lack of) growth of variance over time is investigated.

Chapter 5

Results for the perturbed cases

As the previous chapter shows the critical mixing fraction does not show much variability for the BOMEX case. Since the χ_c is hypothesized to be linked to the entrainment and detrainment (section 3.3.3) it is interesting to get more variablity in χ_c to investigate the relation between χ_c and the entrainment and detrainment. In order to get more variability in the χ_c the methods to perturb the BOMEX case from section 3.3 are used. In section 5.1 and section 5.2 the initial profiles are perturbed by a constant amount and the gradient of the initial profiles is perturbed. These methods are then used as inspiration for the relative humidity sensitivity experiments, from which the results are shown in section 5.3. For these last set of experiments the relationships between the RH, χ_c, entrainment and detrainment are investigated. For the same set the relation between the normalized moist buoyancy deficit and the cloud core cover from Neggers et al. (2009) is tested, since this relation is currently tested to be used in the ECMWF weather forecast model.

5.1 Results for constant perturbations to the BOMEX input profiles

For the first set of experiments the input profiles are perturbed by a constant amount. The perturbations to the input profiles are listed in table 5.1 for the different cases. These cases are picked in such a way that the initial θ_v profile does not change so that the CAPE remains the same, as described in section 3.3.1.

Table 5.1: The four cases for the constant perturbed input profiles.

	$\delta\theta$[K]	δq[g/kg]
case 1	0.04	-0.2
case 2	0.07	-0.4
case 3	-0.07	0.4
case 4	-0.13	0.7

The simulation is then started without extra forcings or nudging (a mechanism that tries to nudge the profiles to a predefined state). It is known that without nudging the profiles of q and θ converge to their original BOMEX profiles over time (Reintjes, 2005). On the other hand, the first 3 hours of the simulation are considered to be the startup phase in this report since the profiles are not in a (near) steady-state yet. To avoid the problem of the converging profiles and the startup phase, the fourth hour of the simulation is analysed. The simulations have dimensions $128 \times 128 \times 80$ gridpoints, $6400 \times 6400 \times 3200$ meters. The main aim is to take a look at the mass flux for each run, since a large perturbation in the (gradient) of the mass flux is what influences the mean state variables the most.

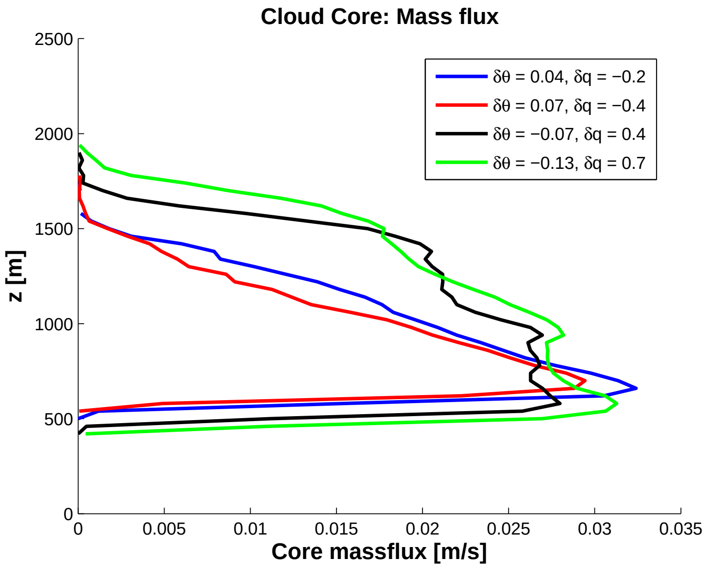

Figure 5.1: The cloud core mass flux profiles for the four cases with constant perturbations to the input profiles of q_t and θ_l from table 5.1. This picture is the average mass flux over the fourth hour.

As can be seen from figure 5.1 the mass flux halfway the cloud changes a factor two between the first two cases from table 5.1 and the second two cases. Considering the small change in the initial profiles this is a large change in the mass flux, but as can be observed from figure 5.1 the gradient of the mass flux profiles in the cloudlayer does not show much change. When observing χ_c not much change is visible either, so although the magnitude of the mass flux shows significant change this is not enough to get more variability in χ_c.

5.2 Results for perturbed input profiles gradients

Another method to perturb the initial profiles is by changing the gradients of the input profiles in the cloud layer and higher. The different cases are listed in table 5.2. These cases are picked in such a way that the gradient of the initial θ_v profile does not change so that the CAPE remains the same, as described in section 3.3.2.

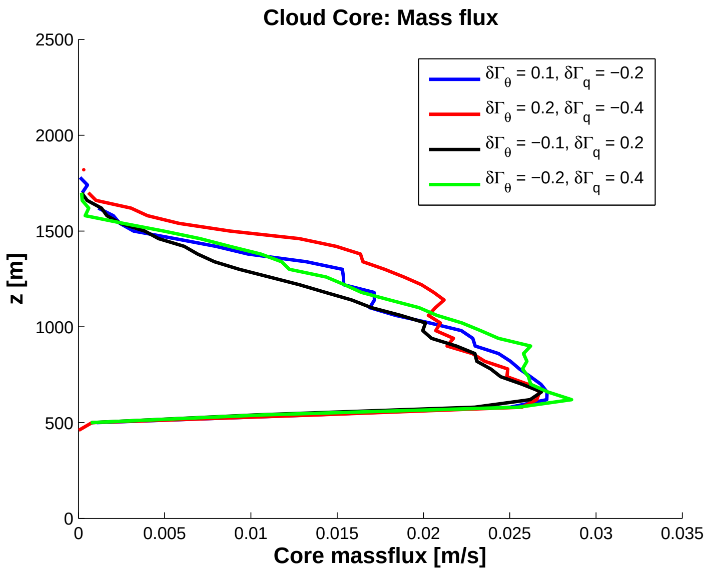

Figure 5.2: The vertical mass flux profiles for the four cases with perturbations to the gradients of the initial profiles. The cases are listed in table 5.2.

Table 5.2: The four cases for the perturbed gradients.

	$\delta\Gamma_\theta$[K/km]	$\delta\Gamma_q$[g/kg/km]
case 1	0.1	-0.2
case 2	0.2	-0.4
case 3	-0.1	0.2
case 4	-0.2	0.4

The simulations have dimensions $128 \times 128 \times 80$ gridpoints, $6400 \times 6400 \times 3200$ m. Again the startup phase is discarded and the fourth hour of the simulation is analysed to avoid that the profiles converge to the original BOMEX. Figure 5.2 hardly shows any change in the mass flux profiles compared to the change in the previous section, and when briefly examining the χ_c no notable change is observed. It is therefore decided that perturbing the gradients of the initial profiles is less effective than perturbing the initial profiles by a constant amount.

5.3 Relative humidity sensitivity experiments results

As was shown, perturbing the initial profiles of q and θ changes the mass flux profile by a factor two for small perturbations, but the critical mixing fraction does not change. These previous experiments do however give a hint, together with the work from Derbyshire et al. (2004), to investigate the response of the χ_c to a perturbation of the relative humidity (as explained in section 3.3.3). Hopefully the χ_c and also the entrainment show more variablity when perturbing the relative humidity so that the hypothetical relation between χ_c and ϵ can be investigated. Therefore a series of LES experiments is run to investigate the influence of the relative humidity on the dynamics of the BOMEX case.

5.3.1 Perturbed initial profiles

The cases listed in table 5.3 have been picked with the help of figure 3.6. The idea is to change only the relative humidity, always keeping the θ input profiles the same as with the original BOMEX to try to keep the CAPE unchanged. The cases from the table correspond to the cases shown in figure 3.7. The simulations have dimensions $128 \times 128 \times 80$ gridpoints, $6400 \times 6400 \times 3200$ meters. Instead of the surface fluxes, the surface temperature and moisture is prescribed. The variables are sampled every 12 seconds and averaged over the fourth hour of the simulation. These cases are then run two times, one time with the inversion at 1500m height, the same as the standard BOMEX case. Then the cases are also run with an increased inversion at a height of 2500m and an increased simulation domain height to see the effect of a deeper cloudlayer on the analysis. In both cases no nudging is applied.

Table 5.3: The cases for the relative humidity sensitivity experiments.

	RH [%]
case 1	20
case 2	50
case 3	60
case 4	65
case 5	70
case 6	75
case 7	80
case 8	85
case 9	90
case 10	95

The inversion is elevated because it is observed that the inversion influences the cloud layer for cases with high relative humidities. The environment contains a lot of moisture for the cases with high relative humidities, so the evaporation rate of the passive (non-buoyant) clouds near the inversion is very low. This leads to anvil-shaped clouds, with a lot of liquid water located just under the inversion. This liquid water does not contribute to the dynamics in the cloud layer, but can act as noise when calculating cloud statistics. With this in mind, the results shown in the coming paragraphs are from the cases with the elevated inversion. When notable differences are found between the cases with the standard-height inversion and the elevated inversion this is mentioned in the text. The first three hours of the LES are discarded as the LES is still in the startup phase.

5.3.2 Thermodynamic profiles

To get an understanding of the influence the relative humidity has on the thermodynamics of the simulation the results in figure 5.3 are presented. The effect of the perturbed initial q_t profiles is immediately visible on the q_t profiles in the upper right panel of figure 5.3. As is visible in the q_l plot the case with 20% RH does not produce any clouds, and because of that the dry convective boundary layer is extending to up to 1 kilometer instead of 500 meter. At 1 kilometer an inversion starts to form for this case and for the cases with 20 and 50% RH. This inversion is also clearly visible in the θ_l and θ_v plots

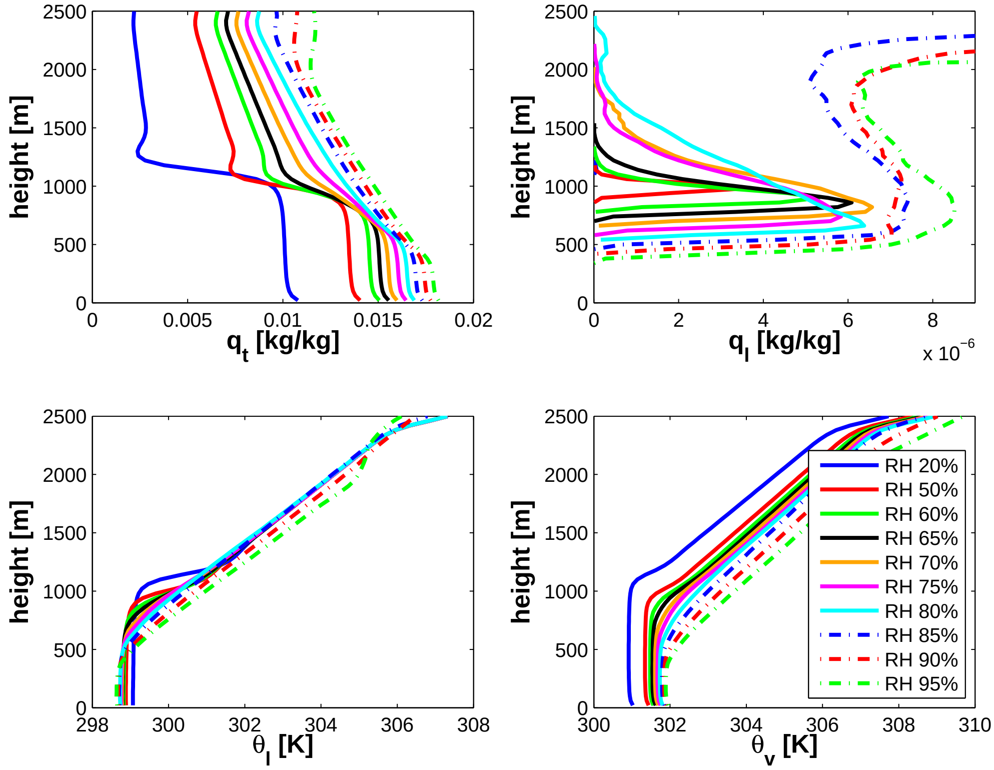

Figure 5.3: The vertical profiles for the total specific humidity (top left), liquid water specific humidity (top right), liquid water potential temperature (bottom left) and the virtual potential temperature (bottom right). The profiles are averages over the fourth hour of the simulation.

as a change in the gradient of the profiles. The θ_v profiles in the cloud layer however do still have more or less the same gradients, which was an aim when perturbing only the relative humidity and not the θ gradient. It is therefore expected that the CAPE and CIN do not change much between the cases. When looking at the q_l profiles it is observed that there is a large difference between the profiles of the cases with relative humidities lower than 85% and those with a relative humidity of 85% and more. The effect of the inversion is visible at 2000 meters and more, the clouds for the cases with a RH of 85% or more show an anvil-like shape. As said before, this anvil-like shape is caused by non-buoyant clouds that have a low evaporation rate due to the high relative humidity. But even when ignoring this anvil-shape the q_l profiles for these high-relative humidity cases still have a very different shape, with a q_l that is 2-3 times larger than for the other cases at a height of 1 kilometer. The standard BOMEX case has a RH of about 75-80%, so a relative humidity of just a few percent higher than the standard BOMEX case allows the formation of 2-3 times more clouds. The q_l for the cases with 85,90 and 95 % RH are again close to eachother, so a transition is just occurring between a RH of 80 and 85 %. Lowering the RH also has an effect on the q_l profile but this effect is a lot smaller.

5.3.3 Mass flux

The thermodynamic profiles show that the formation of clouds is influenced by changing the relative humidity. The plots in the previous paragraph do not give information about the type of clouds, the liquid water that is observed could be from passive (non-buoyant) or active (buoyant) clouds. To distinguish between passive and active clouds the mass flux is examined. The mass flux is depicted in figure 5.4 to see the influence of the RH on the mass flux.

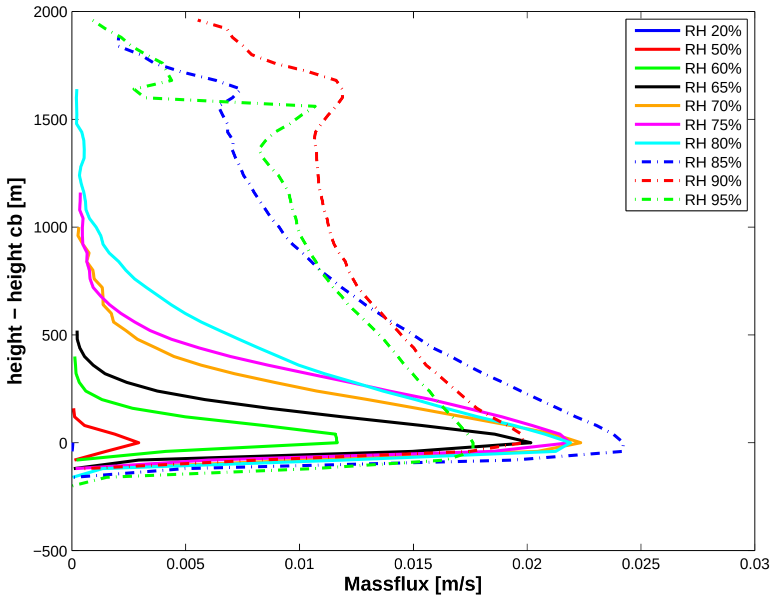

Figure 5.4: The vertical mass flux profiles averaged over the fourth hour for the different runs from table 5.3. The cloudbase is placed at zero height in order to be better able to compare the gradients of the different runs.

As can be seen in figure 5.4, the magnitude of the mass flux varies by a large amount between the runs. The run with a RH of 20% is hardly showing any mass flux at all, which is in agreement with the lack of liquid water in figure 5.3. The gradient of the mass flux of the runs however does not show much change for a RH lower than 80%, but if the RH is higher than 80% the gradients change by a larger amount (figure 5.5). This is in agreement with the q_l profiles from figure 5.3 since a large difference is also observed in the q_l profiles between the 80 and 85% RH cases. The mass flux halfway the cloudlayer is about 2 times larger for the cases with high relative humidities compared to the other cases, so the increase liquid water that is observed in the q_l profiles is mostly due to active clouds.
Near the inversion the q_l profiles show an anvil-like shape, and this shape is also visible in figure 5.4, although the magnitude of the anvil-shape is very small in the mass flux profiles compared to the size of the anvil-like shape in the q_l profiles. This confirms that most cloudpoint in the anvil-like shape are indeed passive and can be ignored when investigating cloud-layer relationships.
Another feature that is visible is that the mass flux at the cloudbase is smaller for the cases with 90 and 95% RH than for the 85% RH case. These cases do however have a smaller gradient than the 85% case, so they have a higher mass flux higher in the

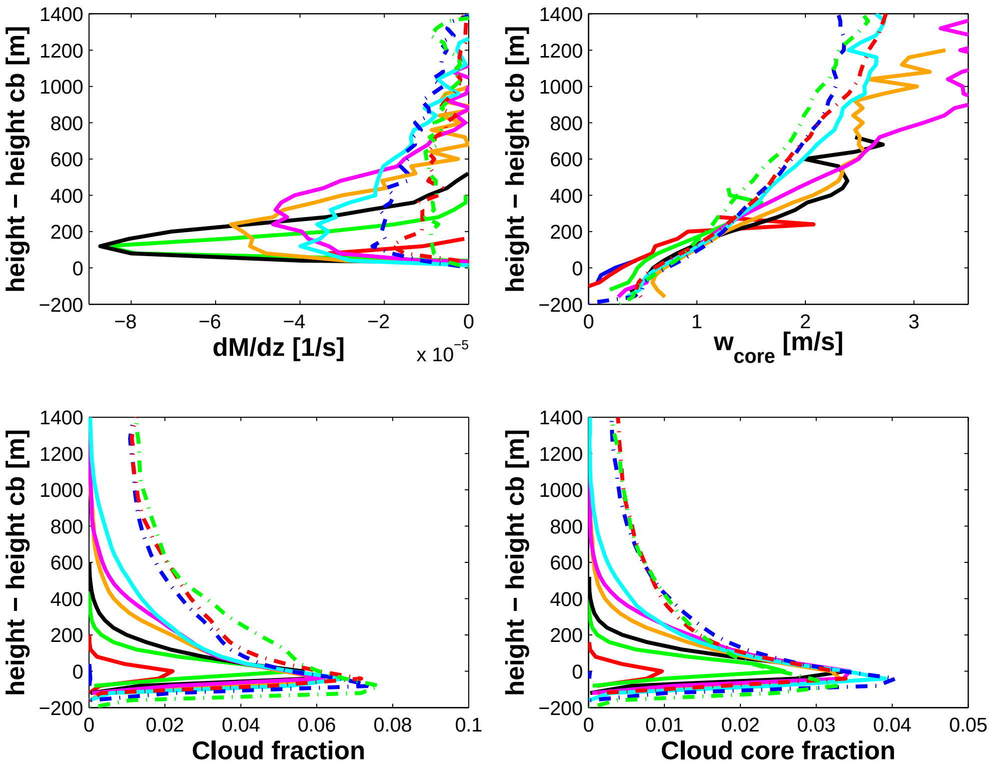

Figure 5.5: The gradient of the mass flux as a function of height (top left), the cloud fraction (top right), the cloud core fraction (bottom left) and the vertical velocity in the core of the cloud (bottom right), averaged over the fourth hour of the simulation. The legend is the same as in figure 5.3.

cloudlayer. In figure 5.5 it can be seen that the cloud fraction is indeed the highest for the runs with the highest RH, but the core fraction is lower for the runs with 90 and 95% RH compared to the 85% run. So this means that the cases with a relative humidity of 90 and 95 % have more passive clouds near the cloudbase, while the run with 85% has more active clouds near the cloudbase. It is probably that this is caused by the extremely high relative humidity, at a RH of 90 or 95 % the environment contains so much moisture that it is very easy for clouds to form, even though not all clouds have a large buoyancy. If a cloud has only a small positive buoyancy it can become non-buoyant after rising only a few meters. Ih the environment would contain only the same amount of moisture as in the standard BOMEX case then these passive clouds would evaporate easily, but since the relative humidity is very high these clouds have a low evaporation rate. Therefore passive clouds can exist longer, which might explain the existence of passive clouds near the cloudbase in the high relative humidity cases. When examining the cloud core cover and the vertical velocity, it is seen that the change of the gradient of the mass flux is mainly caused by the cloud core cover, the gradient of the vertical velocity does not change much. This means that, even though the clouds grow in size, the amount of energy that is converted to vertical velocity does not really change. This can be linked to the fact that the initial θ profile is not perturbed in these cases to try to keep the CAPE unchanged. Figure 5.3 indeed shows that the θ_v gradient does not change much between the cases, so the CAPE is also not expected to change much. This means that the amount of energy in the atmosphere for convection is also nearly the

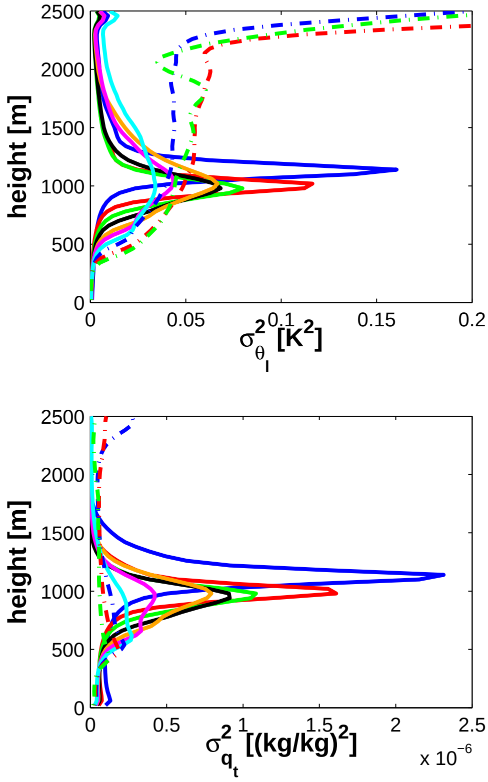

Figure 5.6: The variances for the different thermodynamic variables for the different runs from table 5.3. The values are averages over the fourth hour of the simulation. The legend is the same as in figure 5.3

same for the cases. This is in agreement with the observation that the vertical velocity in the cloud core does not differ much between the cases, since this vertical velocity is generated by the CAPE.

5.3.4 Variance

From the thermodynamic profiles and the mass flux profiles it is clear that changing the relative humidity has a notable effect on the formation of clouds. The question rises what happens to the variances of several dynamic variables in the cloudlayer, since the variance is related to the entrainment and the fluxes as shown in section 2.6.2. The variances are shown in figure 5.6. As can be seen from this picture, the magnitude and gradients of the variances of these thermodynamic variables show a lot of change between the cases. The variance of the total specific humidity in the lower left panel and the vertical velocity in the lower right panel show that the maximum variance is higher for the case with the lowest relative humidity. For the q_t variance this can be explained with the help of figure 5.3. At the height where the variance of q_t peeks is a large change in the vertical profile of q_t, due to the formation of an inversion at this height. The w variance can be explained by the fact that the cloudbase changes when the RH changes, as is visible in figure 5.3, which shows the vertical profiles of some thermodynamic variables. The cloudbase height is increasing as the relative humidity decreases because an undeep cloud layer forms due to the lack of moisture in the air. A higher cloudbase means that the dry convective boundary layer is deeper. It is known that the variance in the subcloud layer scales with (Stull, 1988)

$$\overline{w'^2} = 1.8(\frac{z}{z_i})^{2/3} \cdot (1 - 0.8\frac{z}{z_i}) {w_*}^2 \tag{5.1}$$

where α is a constant depending on the height and the depth of the dry convective boundary layer and w_* is the convective velocity scale, given by (Stull, 1988)

$$w_*^3 = \frac{g}{\overline{\theta_v}} \cdot (\overline{w'\theta'_v}_s \cdot z_i) \tag{5.2}$$

where z_i is the depth of the dry convective layer and $\overline{w'\theta'_v}_s$ is the surface flux of θ_v. Combining equations (5.1) and (5.2) and simplying gives

$$\overline{w'^2} = 1.8z^{2/3} \cdot (1 - 0.8\frac{z}{z_i})^2 \cdot (\frac{g \cdot (\overline{w'\theta'_v})_s}{\overline{\theta_v}})^{2/3} \tag{5.3}$$

This equation implies that the variance increases as the mixed layer depth z_i increases. When looking at the variances of q_t, θ_l and θ_v a maximum in the variances is observed near an inversion that is forming at around 1 kilometer. For the case with a relative humidity of 20% no clouds are forming, but for the cases with a relative humidity of 50 % and higher clouds are forming just below this inversion height. So the formation of clouds coincides with the peek in variance, and since the value of the peek changes up to a factor 3 between the cases it is noted that the variance in the cloudlayer changes by up to a factor 3 due to a change of relative humidity.

5.3.5 Diagnosed entrainment and detrainment

This dependence of the variances in the cloud layer on the change in relative humidity is expected to lead to a change in the entrainment and detrainment since the variance and entrainment/detrainment are linked (section 2.6.2). To investigate the relation between entrainment and detrainment and the relative humidity various plots concerning the diagnosed entrainment and detrainment rates are shown in figure 5.7. The diagnosed entrainment in figure 5.7 is larger near the cloudbase and decreases with height, the diagnosed detrainment shows the opposite behaviour. This behaviour is commonly observed for the standard BOMEX case (Siebesma, 1998).

The high values for the entrainment for the runs with high RH values near the inversion can be explained because of the formation of the anvil-like shaped clouds that were mentioned before. The mass flux profiles showed that most of the cloud point in this anvil-like shape are passive, but some are still active. These active points are sampled to be cloud core points, and are used to calculate a value for the entrainment. The entrainment is a function of the derivative of the total specific humidity in the cloud core as a function of height $\frac{\partial q_{t,c}}{\partial z}$, which is shown in the lower left panel of figure 5.7. As can be seen from this plot the derivative of $q_{t,c}$ is indeed very large just below the inversion, which leads to a very large value for the diagnosed entrainment. However, these anvil-like cloud points are not interesting for the cloud layer dynamics, so the large values for the diagnosed entrainment just below the inversion can be ignored.

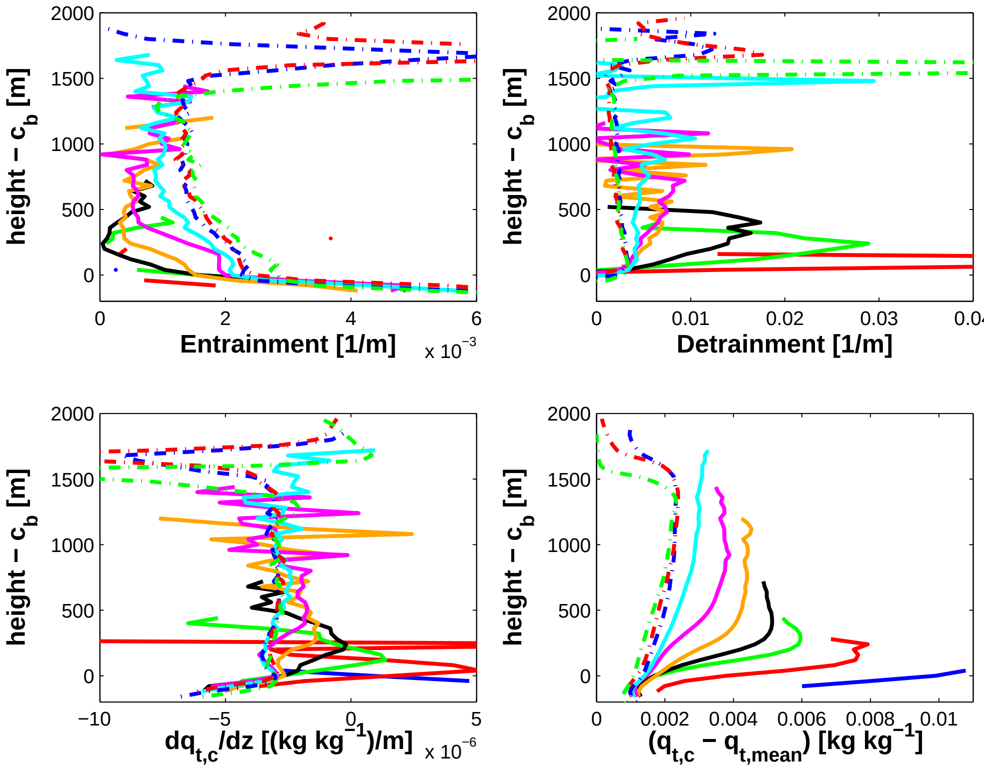

Figure 5.7: The diagnosed entrainment and detrainment rates for the runs from table 5.3. The top left picture shows the diagnosed entrainment as function of height, the top right picture shows the diagnosed detrainment as a function of height. The bottom pictures show the numerator (bottom left) and denominator (bottom right) of equation (2.46). The heights are scaled with the cloudbase, the values are averages over the fourth hour of the simulation. The legend is the same as in figure 5.3.

As can be seen in the lower left panel of figure 5.7 the runs with higher relative humidities have smoother $q_{t,c}$ derivatives in the cloudlayer. A higher relative humidity means that there are more clouds in the ensemble, which explains the smoother derivatives. The average derivative of $q_{t,c}$ does not change much between the different cases, only the spread differs significantly. Since the entrainment is diagnosed by dividing the values from the lower left panel of figure 5.7 with the values on the lower right panel of figure 5.7 this means that the change of magnitude of the entrainment is mainly caused by the values plotted in the lower right panel. Furthermore the profiles plotted in the lower right panel are very smooth, which means that the non-smooth behaviour in the diagnosed entrainment and detrainment is completely due to the roughness of the $q_{t,c}$ derivative. Instead of sampling with the cloud core sampling the scalar sampling from section can be used to try to make the $q_{t,c}$ derivative profiles smoother for all the relative humidities. This should make the diagnosed entrainment profiles also smoother so that more details can be distinguished in the diagnosed entrainment profiles. The entrainment diagnosed with the scalar sampling is shown in figure 5.8 for various decay times of the scalar.

When comparing the different scalar decay times in figure 5.8 it is noted that the decay time of 600 seconds in the upper left panel is clearly too small since the diagnosed entrainment values are too low compared to the diagnosed entrainment found with the cloud core sampling. The cause of the lower values is that scalar decay time is smaller

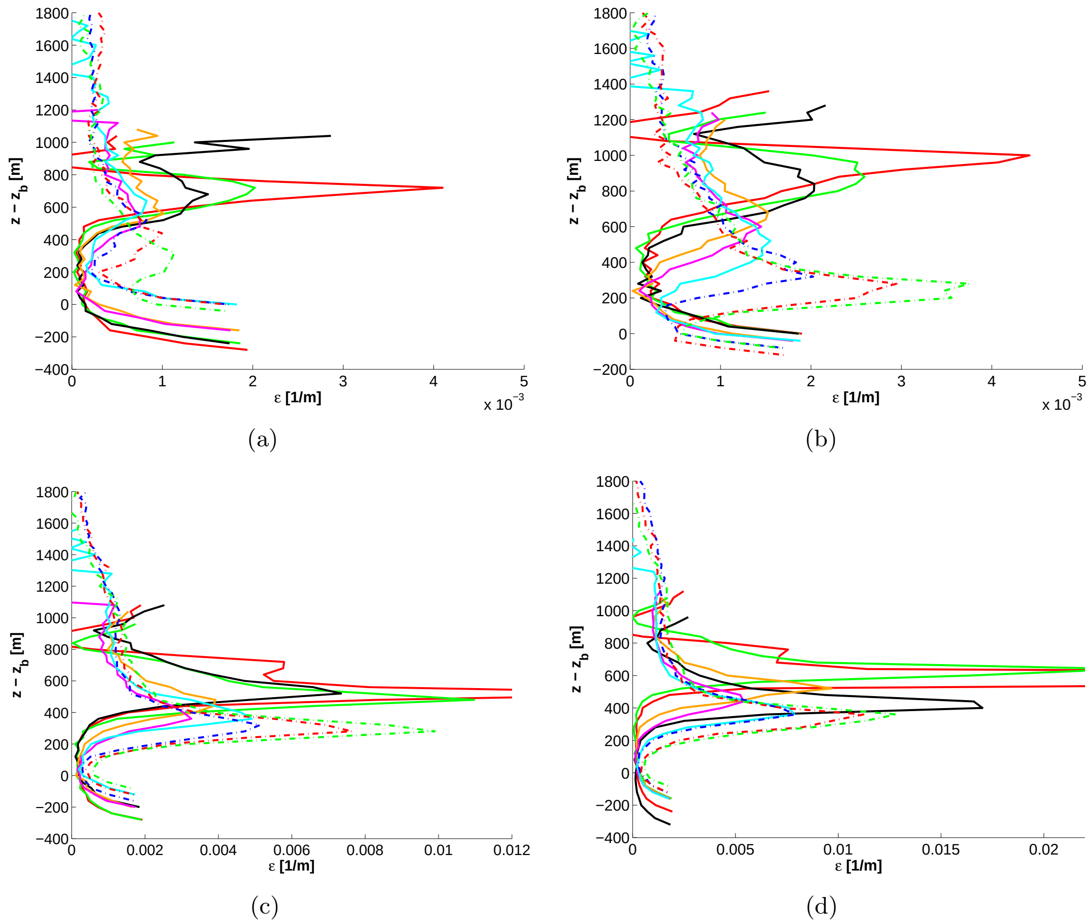

Figure 5.8: The entrainment diagnosed with the scalar sampling for different scalar decay times. The scalar decay times shown here are 600s (top left), 900s (top right), 1350s (bottom left) and 1650s (bottom right). The values are averages over the fourth hour of the simulation. The different lines are from the different RH cases from table 5.3.

than the time it takes the thermals to transport the scalar higher in the atmosphere. Because of this the high entrainment rate near the cloudbase is hardly observed. The cases with lower decay times show a significant peek near 1 kilometer because hardly any clouds form and the mixed layer is reaching up to 1 kilometer. So the scalar is quickly distributed evenly in the mixed layer that reaches up to 1 kilometer because the time to mix the scalar evenly over the layer is small compare to the time it takes the thermals to deposit the scalars in the cloudlayer.

In section 2.5.4 the scalar sampling was tested for the standard BOMEX case, and it was concluded that a scalar decay time of 1350 seconds matches the cloud core sampling best in the cloud layer. The question is wether this decay time of 1350 seconds is universal, or that it changes when perturbing BOMEX. Comparing figure 5.8 and the top left panel of figure 5.7 indicates that the scalar decay time of 1350 seconds still gives results that are closest to the results of the cloud core sampling. Furthermore, comparing the plots in figure 5.8 with figure 5.7 reveals that the scalar sampling indeed produces much smoother entrainment profiles than the cloud core sampling. The profiles for the cases with higher relative humidities still look smoother than the profiles with lower relative humidities, but the heights just below the inversion layer contain almost no roughness anymore,

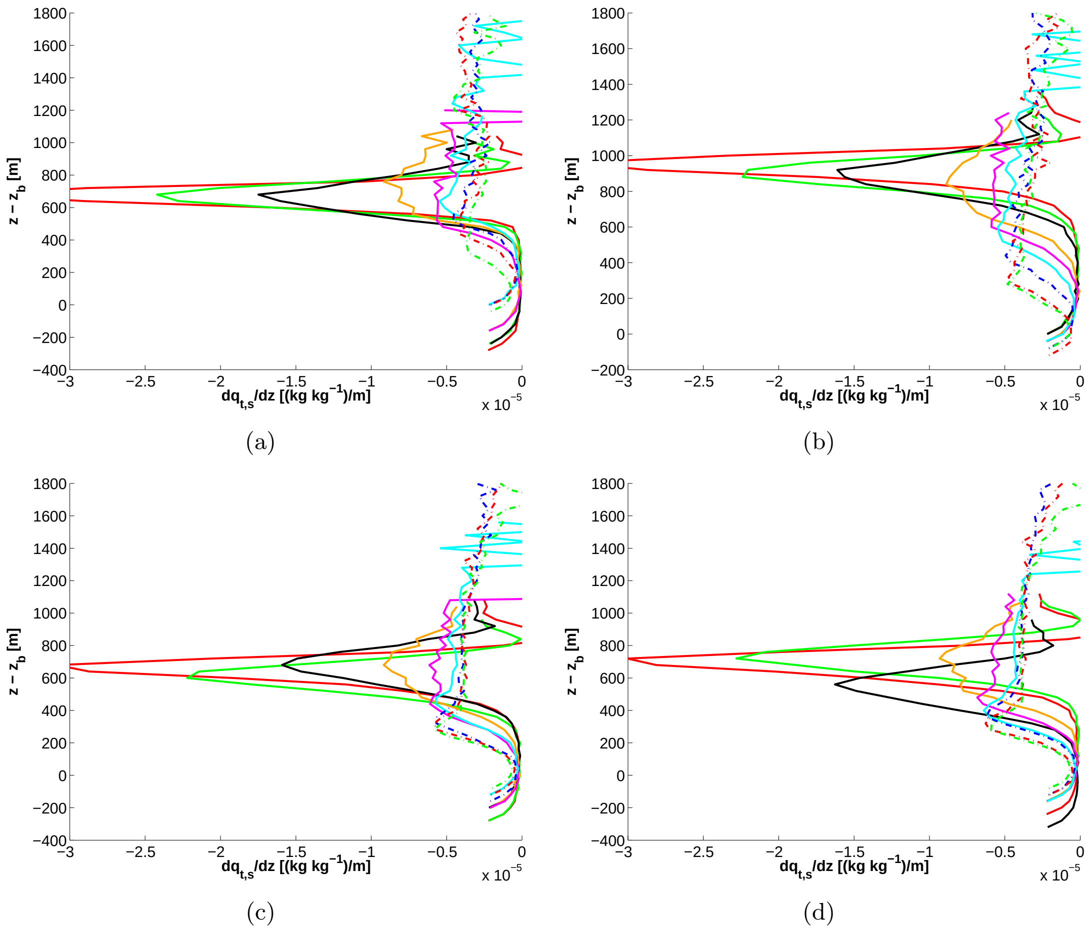

Figure 5.9: The derivative of $q_{t,s}$ as a function of height for different scalar decay times, where the subscript s stands for scalar sampled. The scalar decay times shown here are 600s (top left), 900s (top right), 1350s (bottom left) and 1650s (bottom right). The values are averages over the fourth hour of the simulation. The different lines are from the different RH cases from table 5.3.

which is a clear improvement over the diagnosed entrainment shown in figure 5.7. To see wether the improvements to the smoothness of the profiles are indeed caused by the derivative of $q_{t,s}$ (where subscript s stands for scalar sampled), figure 5.9 is presented. When comparing figure 5.9 to figure 5.7 it is clear that the scalar sampling removes much noise from the plots. The scalar decay time does not have a lot of influence on the values of the derivative $q_{t,s}$, which means that the term $q_{t,s} - q_{t,mean}$ mainly causes the differences between the diagnosed entrainment profiles for the different scalar decay times. Figure 5.10 is presented to see the effect of the relative humidity on the diagnosed entrainment and detrainment, the entrainment and detrainment are diagnosed with the cloud core sampling in these figures. It is interesting to see that the entrainment depends on the relative humidity, and the detrainment seems related to the relative humidity as well. The latter relation is only visible for these runs with the elevated inversion, for runs with the inversion at the same height as the standard BOMEX case this is not visible. It is hard to determine wether the entrainment and detrainment are related to the RH and what the precise relation is because of the spread. Some very high values for the entrainment and detrainment occur near the inversion and may cause part of

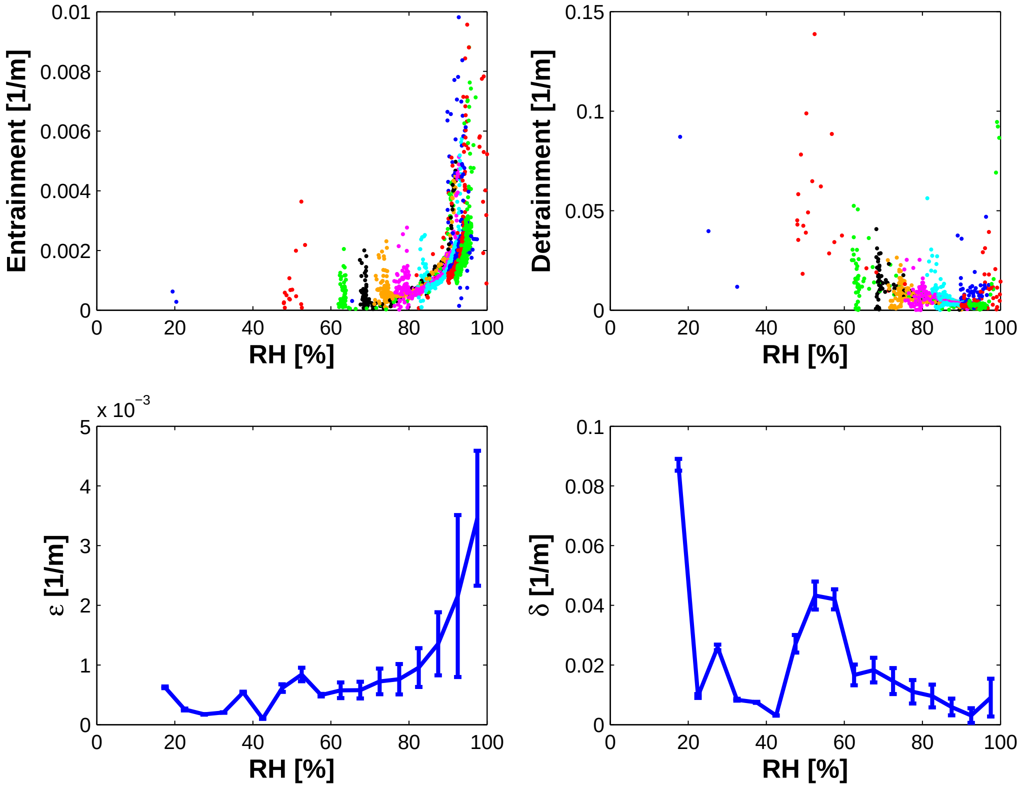

Figure 5.10: The entrainment (left) and detrainment (right) plotted against the relative humidity. The values used to make these plots are hourly averages from hour four to eight of the simulation. The bottom figures are taken from within the cloud layer only. The legend for the upper figures and the colours of the scatterplots corresponds to the legend in figure 5.3

the apparent relationship, and this is not necessarily physical since it concerns isolated points. To get a more precise picture the lower two figures are presented differently; the points are put in bins with a width of 5% RH. The mean and standard deviation in each bin is calculated to obtain the lower two pictures of figure 5.10. Values just below the cloudbase and near the inversion are discarded since diagnosing the entrainment and detrainment can give unphysical results there. From this figure the correlation between the relative humidity and the entrainment is clearly visible but the detrainment does not seem to correlate with the relative humidity. To get more insight in the behaviour of the detrainment more runs are needed in the range 20-50% RH. The dependence of the entrainment on the relative humidity can be explained by remembering that the variance of q_t decreases as the relative humidity increases, as was shown in figure 5.6. Equation (2.57) relates the variance of q_t to the term $q_{t,c} - q_{t,mean}$, which is the denominator in equation (2.46) which is used to diagnose the entrainment. So as the variance of q_t decreases with higher relative humidities, so does $q_{t,c} - q_{t,mean}$, which means that the diagnosed entrainment increases. Physically the relation between the entrainment and relative humidity might be explained by the fact that a higher relative humidity leads to more clouds, which means that there are more turbulent thermals that can entrainment environmental air.

5.3.6 Mean state variables

Because of this apparent relation between the entrainment and the relative humidity, it is interesting to take a look at some mean state variables to see how these correlate with the relative humidity, so that finally the hypothetical relationship between the entrainment and χ_c can be tested, as well as the relationship between the normalized moist buoyancy deficit and the cloud core cover.

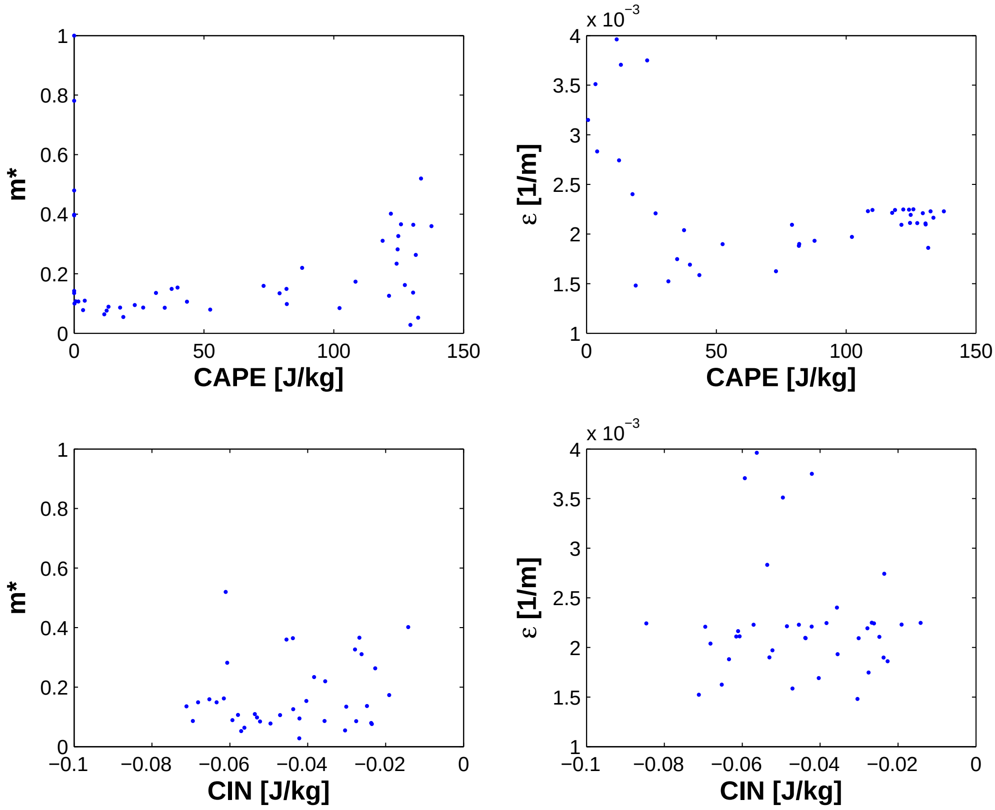

Figure 5.11: The CAPE and CIN vs m^* and the entrainment. The legend is the same as in figure 5.3.

In figure 5.11 the CAPE and CIN are plotted to see if the CAPE and CIN remain unchanged compared to the standard BOMEX case, as was intended. Comparing figure 5.11 with 4.11 reveals that the scatterplots from CAPE seem to be more organized for the perturbed cases than for the original BOMEX case, even though the aim was to keep the CAPE the same as for the original BOMEX. The CAPE that is shown in the upper left panel of figure 5.11 is following a trend that seem more or less the same as the trend that is expected for χ_c against m^*. The entrainment and CAPE also seem to be correlated in a linear way, if ignoring the points with low CAPE since these are from the low RH cases and are more likely to be artifacts since the cloud layer is very shallow and not well-defined. So figures 5.11 and 5.7 show the same picture: if the CAPE increases then so does the entrainment and so does m^* (although the spread is very large). From a physical point of view this is possible because a larger value for the CAPE means that more energy is available for convection, which means that stronger thermals can exist in the cloud layer. These stronger thermals are more turbulent, and turbulence is the

driving force behind the entrainment of environmental air into a thermal.
In figure 5.12 the critical mixing fraction is plotted against several variables. No clear relation between the critical mixing fraction and the relative humidity is visible, although there seems to be a slight increase in χ_c as the RH increases but due to the spread it is hard to quantify this. The relation between χ_c and m^* as shown in the top right panel of figure 5.12 is less clear however. The lower part corresponds well to figure 3.3, but as χ_c increases so does the spread. The general shape however is the same and for the cases with a non-elevated inversion the observed relation between χ_c and m^* corresponds better to figure 3.3. The hypothetical relations (equation (3.31)) between the entrainment, detrainment and χ_c are tested in the lower two pictures of figure 5.12. The hypothesized linear relationship (Bretherton et al., 2004) between ϵ and χ_c^2 is not found in the lower left panel, but this could be due to the spread. If ignoring the high values of the entrainment there seems to be a linear relation between ϵ and χ_c with a slope that is equal to ϵ_0 from equation (3.31). The constant ϵ_0 is fitted to be 0.011 with an error of 0.0023 for these perturbed BOMEX cases. The relationship between the detrainment and χ_c does not seem to exist; the value for δ is nearly constant for all values of χ_c. It is therefore concluded that the hypothetical relationships between the detrainment and χ_c are not found for these perturbed BOMEX cases.

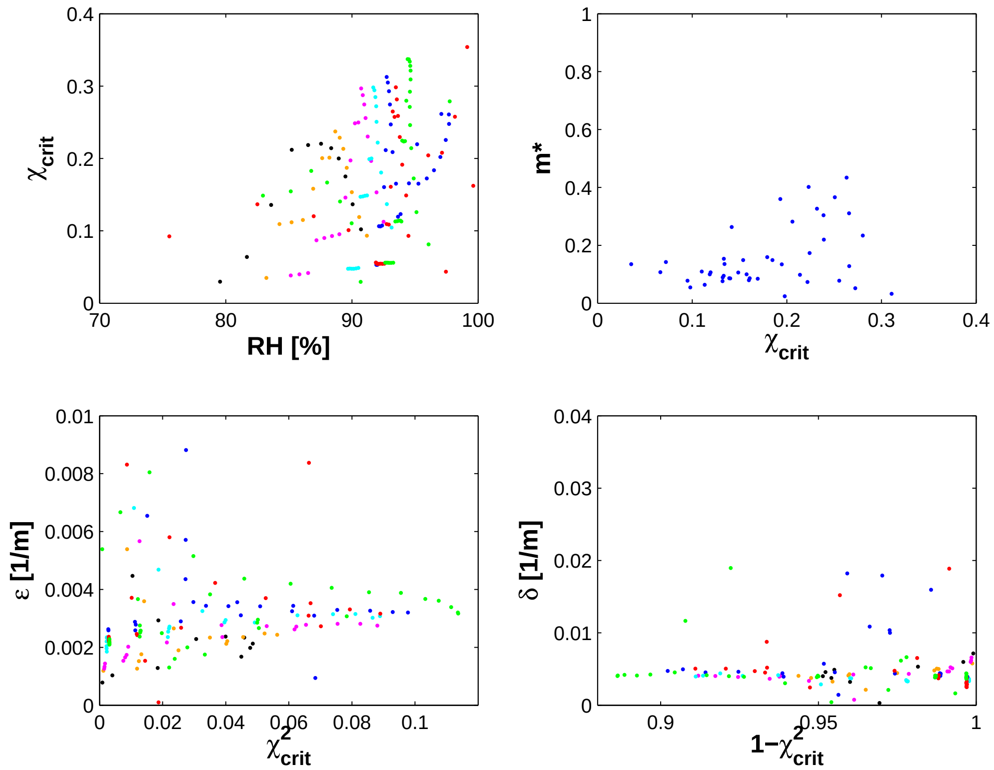

Figure 5.12: The critical mixing fraction plotted in different ways against several variables. The top left figure shows χ_c as a function of the relative humidity. The top right figure shows $\chi_c rit$ as a function of m^*. The bottom figures show the relations between the entrainment and detrainment and χ_c. All values are hourly averages and averaged over the cloud layer.

Since the cloud core cover is found to be the reason behind the observed change in the mass flux profiles, it is interesting to use these perturbed relative humidity simulations to see how the relation between the normalized moist buoyancy deficit Q_c and the cloud core cover a_c behaves, as a correlation between the vertical derivative of Q_c and the vertical derivative of the cloud core cover was found by Neggers et al. (2009).

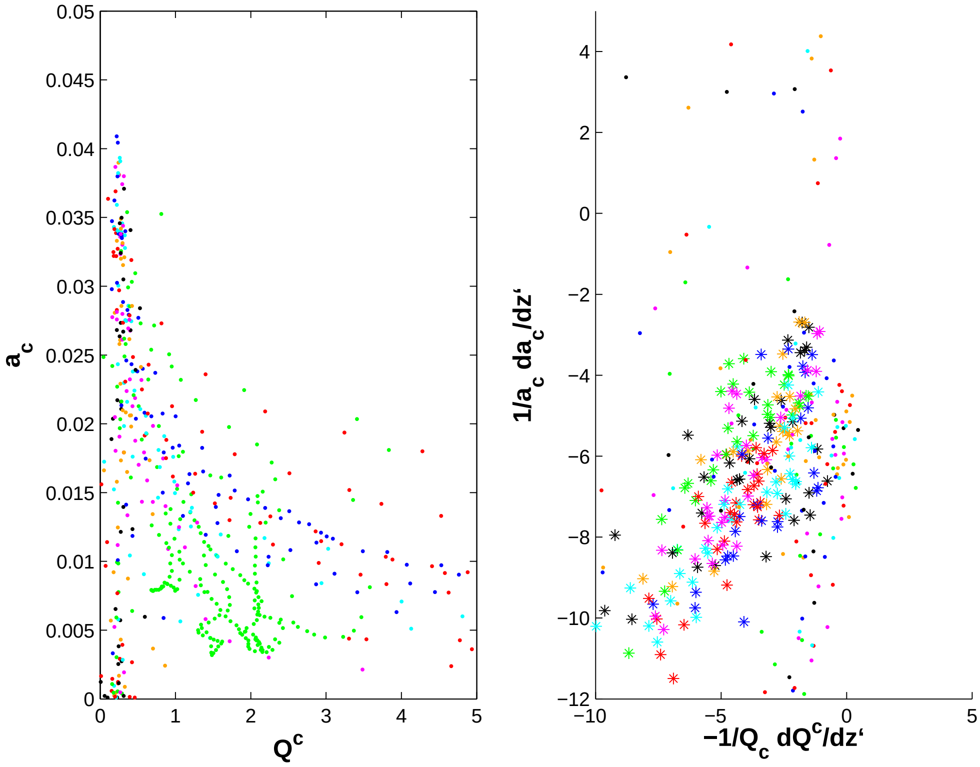

Figure 5.13: Scatterplot of the normalized moist buoyancy deficit as a function of the cloud core cover (left) and the derivatives of these variables on the right. These values are hourly averages from within the cloud layer, the stars in the plot on the right represent the cases with a RH higher than 75%. The colours of the symbols correspond to the colour used in figure 5.3 for the different runs.

Q_c is diagnosed from the LES by equation (3.22). The correlation between the vertical derivates of Q_c and a_c that is seen by Neggers et al. (2009) is not readily visible here for the relative humidity cases because of a large spread. Careful observation reveals that most of the points that are spread around are from the cases with lower relative humidities. Since the cloudlayer that forms in these cases is very shallow, the statistics from these cases might not be very good. Therefore the points from cases with a RH higher than 75% are shown as stars to emphasise the cases with higher relative humidities, the result is shown in figure 5.13. The correlation is now clearly visible, but the prefactor C_a is different from the one found by Neggers et al. (2009). Through a least squares fit the prefactor is in our case estimated to be -1.06 with an error of 0.14. This is different than the prefactor (-1.8) expected from Neggers et al. (2009), but it is the same order of magnitude. When taking a closer look at figure 3.4 the exact locations of the points from the BOMEX case can not be deduced, so it is difficult to compare the results obtained here with the results from Neggers et al. (2009). Since the relation between Q_c and a_c is meant to be used to estimate the cloud core cover in weather forecast models, the implication of a different prefactor is that the gradient cloud core cover is estimated to have a too large value, which means that the cloud core cover is underestimated in the upper part of the cloud layer.

5.3.7 Time-dependence of variances

It is also interesting to take a look at the variances of some thermodynamic variables as a function of time since the variances of the standard BOMEX case do not grow over time, as was found in chapter 4. The question rises if perturbing the standard BOMEX case causes the variance to grow over time, since the vertical profiles of the variances in figure 5.6 show significant variations as the relative humidity changes. To investigate the effect of perturbing the relative humidity of the BOMEX case on the time-dependence of the variance, 10-minute averages of the variances of some dynamic variables taken from halfway the cloud layer are shown in figure 5.14.

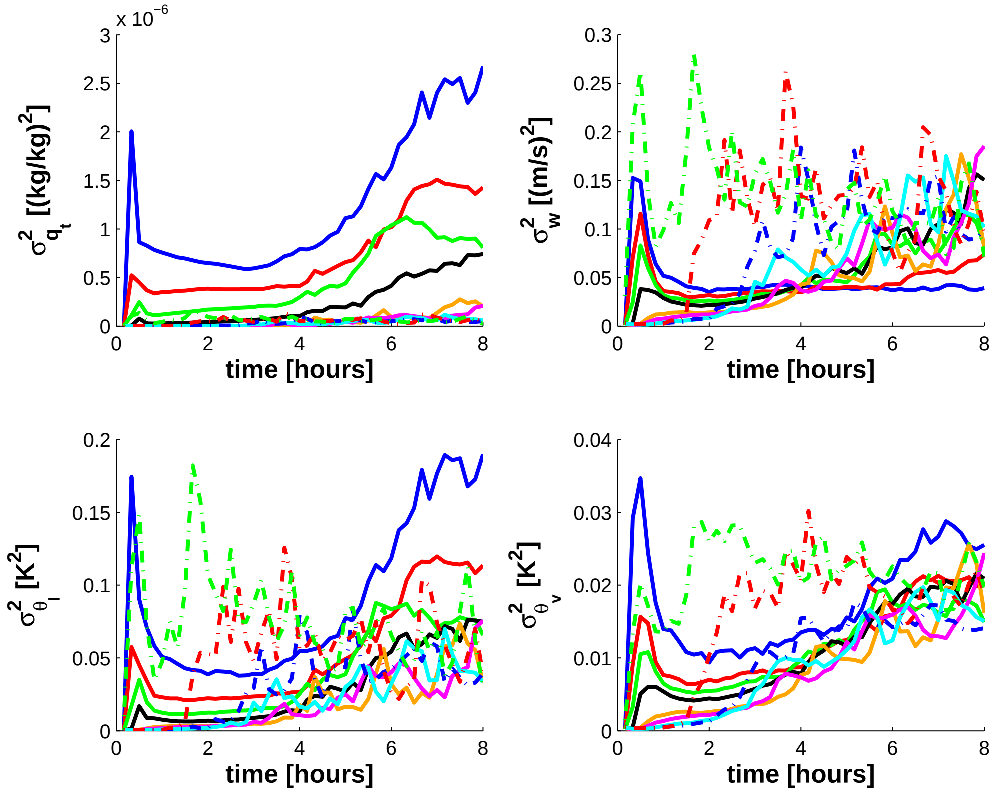

Figure 5.14: Variances of q_t (top left), w (top right), θ_l (bottom left) and θ_v (bottom right) taken halfway the cloud layer. The results represent 10 minute averages. The legend is the same as in figure 5.3.

It is immediately clear why the first three hours of the simulation are usually discarded, the behaviour of the variances in the first three hours is very different from the trend the variances follow after the first three hours. The variances of w, θ_l and θ_v for the runs with the highest relative humidities are behaving different than the variances from the other runs, a lot of noise is visible during the first five hours. This might be an indication for a longer startup phase for the runs with high relative humidities. All variances show growth over time between the third and the sixth hour, but after that the growth seems to stop for the runs with 50%(red line) and 60%(green line) relative humidity. Unfortunately, longer runs are needed to be able to see if the growth of

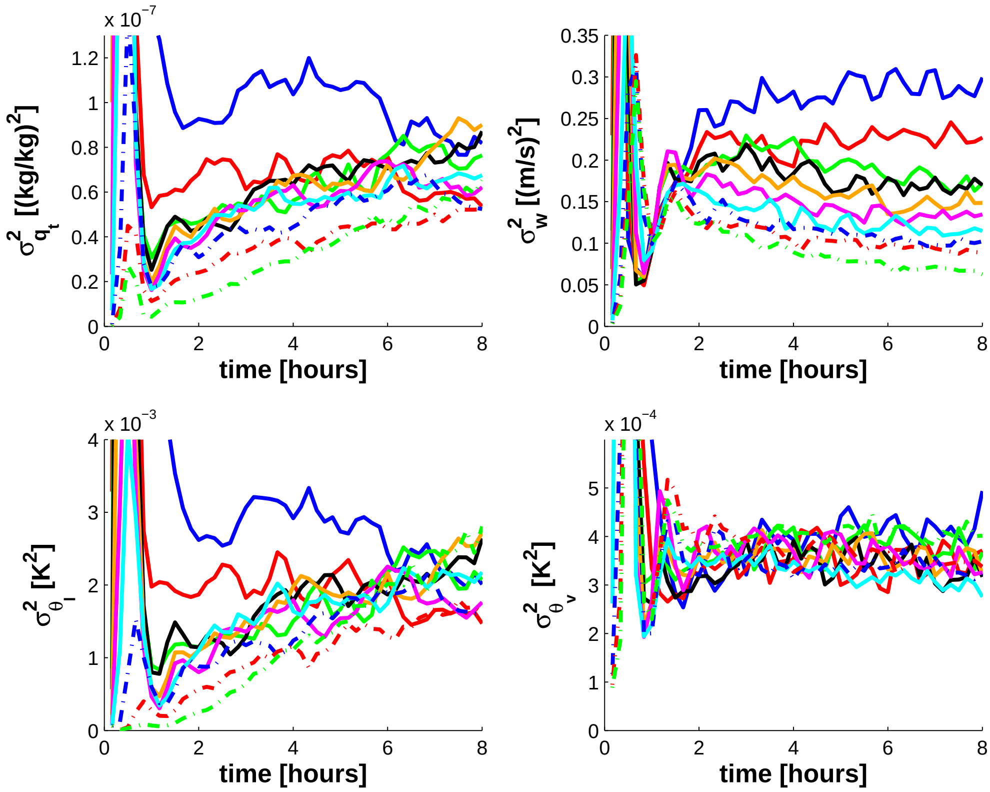

Figure 5.15: Variances of q_t (top left), w (top right), θ_l (bottom left) and θ_v (bottom right) taken halfway the mixed layer. The results represent 10 minute averages. The legend is the same as in figure 5.3.

variance really stops. The black and orange lines represent runs with 55% and 60% RH and show growth of all variances up to the eight hour, but it is again hard to tell what the long-term behaviour is since the simulation only has a length of eight hours. The blue line follows other trends than the other runs, this blue line represents the run with 20% RH. This can be explained with the help of the large jump in the q_t profiles as shown in figure 5.3, since a large jump leads to a large variance. The growth of the variance of q_t and θ_l reminds of the growth of length scales that is observed (Jonker et al., 1999) in the mixed layer. To determine whether this is true, figure 5.15 is presented. This figure shows the variances as a function of time taken at halfway the mixed layer. Comparing figure 5.15 with figure 5.15 does not indicate that the variances of the run with 20% RH are similar halfway the cloud layer and halfway the mixed layer. Furthermore, the variances of q_t and θ_l for all runs grow over time, except for the run with 20% RH. A decreasing variance of this run could indicate that the height of the mixed layer is decreasing over time for this run, since the magnitude of the variance in the mixed layer is coupled to the depth of the mixed layer through equation 5.3. This also means that the mixed layer depth for the other runs is steadily growing since the variances of θ_l and q_t grow over time. The top right panel and bottom right panel of figure 5.15 show that the variances of w and θ_v are not changing over time for any of the runs.
Comparing these results with the results presented in Jonker et al. (1999) show that the results are very similar. In Jonker et al. (1999) only results for w and θ are presented, the variance of w does not show a time-dependence at all in the dry convective boundary

layer. The variance of θ shows a slight growth as a function of time. Comparing the results from figure 5.14 and 5.15 with the results from de Roode et al. (2004) shows that the results are very similar. In de Roode et al. (2004) a growth as a function of time of the variance of q_t and θ_l in the mixed layer is found, but not for θ_v and w, which is exactly what is also seen in figure 5.15. de Roode et al. (2004) also investigates the time-dependence of variances for a stratocumulus-topped boundary layer, and finds that only the variance of w does not show a growth as a function of time, while the variances of q_t, θ_l and θ_v do due to a growth of scales. The same behaviour of the variances of these variables is found in figure 5.14, which means that perturbing the BOMEX case allows the variances and thus scales to grow as a function of time.

Chapter 6

Conclusions and discussion

This chapter is divided into two parts. Part 1 gives the conclusions and some discussion for the results that were presented in chapter 4 and chapter 5. The second part gives recommendations based on the conclusions of this report.

6.1 Conclusions and discussion

6.1.1 Subdomain analysis

No clear scale-dependence is observed for the shallow cumulus BOMEX case.
The variances of the humidities and the potential temperatures do not show a dependence on the domainsize (scale) for the shallow cumulus BOMEX case, as opposed to the stratocumulus FIRE case. This seems to be related to the lack of growth of the variances as a function of time for the shallow cumulus BOMEX case, since this growth is observed for the stratocumulus FIRE case. The growth of the variances of the humidities and the potential temperatures for the stratocumulus FIRE case known from measurements is confirmed with DALES. The standard deviation of the saturation excess s scales with the domain size with a power law, the coefficient in the exponent β_s is found to be 0.26 from the LES results which is close to the constant $\beta_s = 1/3$ found by Wood et al. (2002).
The diagnosed entrainment and detrainment rates, as well as the CAPE and CIN and the critical mixing fraction do not show a clear correlation with the subdomain size. For all these variables the same behaviour is observed: for smaller subdomain sizes some changes are visible, but the spread in the variables is too large to see a relation with the subdomain size. This large spread means that the value of a variable can have very different values on different subdomains, but that the average over all the subdomains does not change much.
The large spread of the entrainment, detrainment and CAPE and CIN on the small subdomains can be explained by the fact that a single subdomain can contain a very specific cloud, or even just a small part of a cloud. For the entrainment this means that the cloud points in the subdomain can be almost completely passive, leading to a very small entrainment rate. On the other hand, very active clouds in a subdomain can lead to high values for the entrainment. For the detrainment the same applies, but the other way around.
Cloud core points with a very large or small positive buoyancy can cause the critical mixing fraction to have large variations, since a cloud point that has only a small positive

buoyancy only needs a small amount of environmental air to become neutrally buoyant, thus having a small critical mixing fraction. Cloud points that have a large positive buoyancy need to be mixed with a lot of environmental air to become neutrally buoyant, thus having a large critical mixing fraction.
The large variations in CAPE and CIN on the smallest subdomain sizes mean that the energy available for convection on the smaller subdomains individually differs. Apparently local differences in temperature can lead to a different build-up of CAPE or CIN on a single subdomain which leads to the large variation in values. The existence of these local differences is of course confirmed by the fact that cumulus clouds only form at certain position due to thermals at certain locations.
Initially the correlation between the critical mixing fraction χ_c and m^* from de Rooy and Siebesma (2007) was also not clear. This correlation is found to be only visible when time-averaging over enough time samples, but the variation in χ_c is too small for the standard BOMEX case to validate the entire shape of the correlation from figure 3.3.

6.1.2 Perturbed cases

Perturbing BOMEX by setting the relative humidity to a certain amount in the initial profiles produces a wide range of mass flux profiles. The changes in the mass flux profile are mainly caused by the cloud core fraction, a higher relative humidity causes a higher cloud core cover, which means that more clouds exist at a certain height. It is found that the cloud core cover only changes at levels higher than the cloudbase, but that the cloud core cover at the cloud base itself does not change when increasing the relative humidity. This means that the number of thermals that can gather enough momentum to become a cloud stays the same, while the depth of the clouds in the cloudlayer increases. This is of course consistent with the fact that the gradient of the virtual potential temperature was not changed so CAPE and CIN do not change much, so the amount of energy a thermal needs to overcome to become a cloud (CIN) does not change. The higher relative humidity leads to a lower evaporation rate of the clouds in the cloud layer, which means that the clouds become deeper.
The entrainment is found to be a function of the relative humidity, but no clear correlation between the detrainment and the relative humidity is observed. As the relative humidity increases so does the entrainment, this relation is non-linear. A higher RH means that the environment around the cloud contains more moisture, so the thermodynamic properties of the environment are closer to the properties of the cloud. This probably makes it easier for the cloud to entrain this environmental air, while it is harder for the cloud to detrain cloudy air since the cloudy air has a lower evaporation rate. However, the relation between the detrainment and the relative humidity is unclear because no information is available between 20 and 50% RH. *The scalar sampling method from Couvreux et al. (2009) can be used to diagnose the entrainment in the subcloud layer and gives smoother entrainment profiles for the cases with lower relative humidities and just below the inversion.* The improvements in the area just below the inversion are caused by a smoother derivative of the sampled total specific humidity $\frac{\partial q_{t,s}}{\partial z}$ compared to the cloud core sampling. This scalar sampling method also provides information about the entrainment in the subcloud layer. The scalar decay time of 1350 seconds that was found to match the cloud core sampling closely in the cloud layer for the standard BOMEX case also matches the cloud core sampling well in the cloud layer for the perturbed cases.
The hypothesis suggesting that the entrainment and detrainment scale with resp. the

square and 1 minus the square of the critical mixing fraction χ_c *as suggested by Bretherton et al. (2004) is only observed for the entrainment for the perturbed BOMEX cases.* The detrainment does not show a relation with χ_c, but seems to be almost a constant. The prefactor ϵ_0 is fitted to 0.011, which means that the entrainment is increasing as the critical mixing fraction increases. The critical mixing fraction is a measure of how much environmental air is needed to make an updraft parcel neutrally buoyant, the entrainment is a measure of the amount of air flowing into the updraft. So an increasing buoyancy of the updraft compared to the environment is coupled to an increasing flow of environmental air into the updraft. This seems logical because nature tries to even out the buoyancy difference between the updraft and environment by increasing the flow of environmental air into the updraft to decrease the buoyancy of the updraft. The relation between χ_c and the convection response m^* is more clearly observed for the perturbed cases since χ_c now also assumes lower values for the cases with lower relative humidities. The relation between the normalized moist buoyancy deficit Q_c and the cloud core fraction a_c is not immediately visible when using all the perturbed cases available. *When selected only the cases with relative humidities higher than 80% the correlation is found although the prefactor* C_a *found in this research (-1.06) differs from the one found by Neggers et al. (2009) (-1.8).* This leads to an overestimation of the gradient the cloud core fraction in the original model, which means that the cloud core fraction is underestimated in the upper part of the domain. Since this relation is intended to be used in weather forecast models to estimate the cloud core fraction this difference could be important.

A dependence of the variances of moisture and potential temperatures on the time is found. Initially a growth is observed, but near the end of the simulation runtime the growth as a function of time for the variances for some of the RH cases seems to stop. Longer simulation are needed for conclusive results.

6.2 Recommendations

6.2.1 Implications of the results of the subdomain analysis

It was shown that the slab-averaged value of the entrainment and detrainment stay nearly the same as the domainsize decreases. The spread on each subdomain is increasing as the subdomain size decreases, which is due to local differences. For a large-scale model this means that parametrizing the average value of the entrainment and detrainment does not need to be changed as the resolution is increased, but perhaps the increasing spread in the entrainment and detrainment needs to be included when parametrizing them. This could be done by analysing with a LES how the spread of these variables behaves by finding a standard deviation of this spread for different subdomain sizes. The results from this analysis could lead to a statistical model for the spread, which can then be used in the parametrization of the entrainment and detrainment in a high resolution large-scale model. The same process can of course be repeated for any other parametrized variable that behaves in the same way as the entrainment and detrainment when the resolution of the model changes. In this way the fluctuations on the smaller scales that influence the individual grid-boxes of the large-scale simulation can be accounted for in the parametrization schemes.

6.2.2 Discussing the results from the perturbed cases

The hypothetical relations (Bretherton et al., 2004) between the critical mixing fraction χ_c and the entrainment, and χ_c and the detrainment are not found for the BOMEX cases for which the relative humidity is perturbed. The relations could simply not exist at all, or they could just not be existing for this specific combination of cases. It is therefore too soon to dismiss the existence of the relations between χ_c and the entrainment/detrainment. The standard BOMEX case does not seem suited for investigating the relations, since the variability of χ_c is very small, therefore it is recommended to use other shallow cumulus cases that have a natural large variability in χ_c and use a LES to examine the relations.

The scalar sampling method from Couvreux et al. (2009) is found to produce similar results when diagnosing the entrainment to the cloud core sampling in the cloud layer, and greatly improves the profile of the diagnosed entrainment in the area below in the inversion. Since it also provides information about sampled variables in the subloud layer (which is not possible with the cloud core sampling), it is suggested that the scalar sampling is implemented in DALES in the same way the other sampling methods have been implemented. Perhaps it could be tested in more extent first to confirm the similar behaviour of the scalar sampling to the cloud core sampling in the cloud layer for various sampled variables, since this report only focuses on the entrainment.

Another (important) result of the relative humidity experiments is that a smaller prefactor C_a was found for the relation between the normalized moist buoyancy deficit Q_c and the cloud core fraction a_c. This means that the original model overestimates the vertical gradient of the cloud core fraction, which means that the cloud factor is underestimated in the upper part of the cloud layer. This relation is intended to be used in weather forecast models to improve the forecasts, so the implications of this different prefactor could be very important. When looking closely at the original findings by Neggers et al. (2009) (figure 3.4) the data collapse is clearly visible, but it is also noted that the points from some cases seem to follow a different relation. This could suggest that the prefactor found by Neggers et al. (2009) is not an universal constant, but only applies to certain cases. It is therefore interesting to use a LES to investigate for a large number of cases how the relation between Q_c and a_c behaves for each case individually. Hopefully this can be used to get more certainty about the behaviour of the relation between Q_c and a_c for different cloud regimes so that it can be used to improve the weather forecasts.

Bibliography

B.A. Albrecht, D.A. Randall, and S. Nicholls. Observations of marine stratocumulus clouds during fire. *Bulletin of the American Meteorological Society*, 69:618–626, 1988.

B.A. Albrecht, C.S. Bretherton, S. Johnson, W.H. Scubert, and A.S. Frisch. The atlantic stratocumulus transition experiment - astex. *Bulletin of the American Meteorological Society*, 76:889–904, 1995.

Graig F. Bohren and Bruce A. Albrecht. *Atmospheric thermodynamics*. Oxford University Press, 1998.

C.S. Bretherton, J.R. McCaa, and Herve Grenier. A new parameterization for shallow cumulus convection and its application to marine subtropical cloud-topped boundary layers. part i: Description and 1d results. *Monthly Weather Review*, 132:864–882, 2004.

F. Couvreux, F. Hourdin, and C. Rio. Resolved versus parametrized boundary-layer plumes. part i: a parametrization-oriented conditional sampling in large-eddy simulations. *Boundary Layer Meteorology*, 2009.

J.W.M. Cuijpers and P. Bechtold. A simple parametrization of cloud water related variables for use in boundary layer models. *Journal of the Atmospheric Sciences*, 52: 2486–2490, 1995.

Jordi Vila-Guerau de Arellano. Role of nocturnal tubrulence and advection in the formation of shallow cumulus over land. *Quarterly Journal of the Royal Meteorological Society*, 133:1615–1627, 2007.

S.R. de Roode. Thermodynamics of cumulus clouds. *Fisica de la Tierra*, 19:175–188, 2007.

S.R. de Roode. *Syllabus Boundary Layer Clouds*, 2004.

S.R. de Roode, P.G. Duynkerke, and H.J.J. Jonker. Large-eddy simulation: How large is large enough? *Journal of the Atmospheric Sciences*, 61:403–421, 2004.

S.R. de Roode, S. Axelsen, and A.P. Siebesma. The role of the mean relative humidity on the dynamics of shallow cumuli - les sensitivity experiments. Presentation at GCSS Athens, May 2005.

W.C. de Rooy and A.P. Siebesma. A simple parametrization for detrainment in shallow cumulus. *American Meteorological Society*, 136:560–576, 2007.

J.W. Deardorff. Three-dimensional numerical modeling of the planetary boundary layer. American Meteorological Society, 1973. Workshop on micrometeorology.

S. H. Derbyshire, I. Beau, P. Bechtold, J.-Y. Grandpeix, J.-M. Pirou, J.-L Redelsperger, and P.M.M. Soares. Sensitivity of moist convection to environmental humidity. *Quarterly Journal of the Royal Meteorological Society*, 130:3055, 2004.

J-L. Dufresne and S. Bony. An assessment of the primary sources of spread of global warming estimates from coupled atmosphereocean models. *Journal of Climate*, 21: 51355144, 2008.

ECMWF. Operational grid, June 2007. URL `http://www.ecmwf.int/products/data/technical/wam/representations.html`.

T. Heus. *On the edge of a cloud*. PhD thesis, Delft University of Technology, 2008.

H. Jonker. *Clear and cloud-topped boundary layers: two analysis of LES data.* International Summer School Session on Atmospheric Boundary Layers, 2008.

H.J.J. Jonker, P.G. Duynkerke, and J.W.M. Cuijpers. Mesoscale fluctuations in scalars generated by boundary layer convection. *American Meteorological Society*, 56:801–808, 1999.

P.K. Kundu and I.M. Cohen. *Fluid Mechanics*. Academic Press, 2008.

G. Lenderink and E. van Meijgaard. Increase in hourly precipitation extremes beyond expectations from temperature changes. *Nature Geoscience*, 1:511–514, 2008.

R.A.J. Neggers, M. Khler, and A.C.M. Beljaars. A dual mass flux framework for boundary layer convection, part 1: transport. *Journal of the Atmospheric Sciences*, 66: 1465–1487, 2009.

D.A. Randall, Q. Shao, and C.-H. Moeng. A second-order bulk boundary-layer model. *Journal of the Atmospheric Sciences*, 49:1903–1923, 1992.

B. Reintjes. Shallow cumulus clouds. Master's thesis, Delft University of Technology, 2005.

A.P. Siebesma. Bomex shallow cumulus case, July 1997. URL `http://www.knmi.nl/~siebesma/gcss/bomexcomp.init.html`.

A.P. Siebesma. *Buoyant Convection in Geophysical Flows*, volume 513, chapter Shallow Cumulus Convection., pages 441–486. Kluwer Academic, 1998.

Roland B. Stull. *An Introduction to Boundary Layer Meteorology.* Kluwer Academic Publishers, 1988.

M. van Zanten. *Entrainment processes in stratocumulus.* PhD thesis, Delft Universiteit of Technology, 2000.

R. Wood, P.R. Field, and W.R. Cotton. Autoconversion rate bias in stratiform boundary layer cloud parametrizations. *Atmospheric Research*, 65:109–128, 2002.

Appendix A

Overview of used symbols / Abbrevations

Table A.1: An overview of the symbols used in this report. If applicable, the value for a constant is given.

Symbol	Description	Value	Unit
a_c	Cloud fraction		
C_{pd}	Specific heat capacity at constant air pressure for dry air	1005	J kg^{-1} K^{-1}
C_{pv}	Specific heat capacity at constant air pressure for water vapor	1870	J kg^{-1} K^{-1}
C_l	Specific heat capacity for liquid water	4190	J kg^{-1} K^{-1}
D	Lateral detrainment rate		
E	Lateral entrainment rate		
g	Gravitational acceleration	9.81	m s^{-2}
h_d	Dry static energy		kJ kg^{-1}
h_l	Liquid water static energy		kJ kg^{-1}
L_v	Latent heat of vaporization at 273.15 K	$2.5{\cdot}10^6$	J kg^{-1}
M	Massflux		m s^{-1}
m^*	Convection Response		
p_0	Reference pressure	1000	hPa
q_l	Liquid water specific humidity		kg kg^{-1}
q_s	Saturation-specific humidity		kg kg^{-1}
q_t	Total water specific humidity		kg kg^{-1}
q_v	Water vapor specific humidity		kg kg^{-1}
R_d	Gas constant for dry air	287.05	J kg^{-1} K^{-1}
R_v	Gas constant for water vapor	461.50	J kg^{-1} K^{-1}
s	Diff. between the thermodynamic state and the sat. curve		g kg^{-1}
sv	Scalar concentration		
t	Time		s
T	Temperature		K
v_l	Specific volume of liquid water		m^3
v_v	Specific volume of water vapor		m^3
u, v, w	Horizontal(u,v)/vertical(w) wind velocity		
x, y, z	Cartesian coordinates		m
z^{**}	Threshold for the bivariate scalar sampling		m
χ	Mixture fraction		
δ	Fractional detrainment rate		m^{-1}
ϵ	Fractional entrainment rate		m^{-1}
ϵ	R_d/R_v	0.622	
Γ	Adiabatic lapse rate		K km^{-1}
κ	R_d/C_{pd}	0.286	
λ	R_v/R_d - 1	0.61	
π	Exner function		
ρ	Density		kg m^{-3}
ρ_v	Density of water vapor		kg m^{-3}
σ	Cloud cover		
σ	Standard Deviation		
τ	Decay time of a tracer		s
θ	Potential temperature		K
θ_l	Liquid water potential temperature		K
θ_v	Virtual potential temperature		K

Table A.2: An overview of the abbrevations used in this report.

Abbrevation	Full name
ASTEX	Atlantic Stratocumulus Experiment
BOMEX	Barbados Oceanographic and Meteorological Experiment
CAPE	Convective Available Potential Energy
CIN	Convective Inhibition
CRM	Cloud Resolving Model
DALES	Dutch Atmospheric Large-Eddy Simulation
DNS	Direct Numerical Simulation
FIRE	First ISCCP Regional Experiment
IPCC	Intergovernmental Panel on Climate Change
LCL	Lifting Condensation Level
LES	Large-Eddy Simulation
LFC	Level of Free Convection
LNB	Level of Neutral Buoyancy
PDF	Probability Density Function
SCM	Single Column Model